# A new etalon geometry: The spiral phase plate etalon

by

Yisa S. Rumala

A dissertation submitted in partial fulfillment
of the requirements for the degree of
Doctor of Philosophy
(Applied Physics)
in The University of Michigan
2012

Doctoral Committee:

Assistant Professor Aaron E. Leanhardt, Chair
Professor Paul R. Berman
Assistant Professor Tal E. Carmon
Professor Georg A. Raithel
Professor Stephen C. Rand

Everything that is really great and inspiring is created by the individual who can labor in freedom - Albert Einstein, 1938

To my family, friends, teachers and mentors.

# ACKNOWLEDGEMENTS

I would like to acknowledge my PhD dissertation committee: Aaron Leanhardt, Paul Berman, Tal Carmon, Georg Raithel, and Steve Rand. My primary graduate school research adviser is Aaron Leanhardt. As the first student to join his group in 2007, I saw how an empty research lab underwent renovation and grew into a fully functional lab with multiple experimental set-ups and lasers. I worked with Aaron in setting up the lab, constructing apparatus, and performing spectroscopy on ytterbium atoms. This was a significant amount of work in a short time. It was a pleasure working on these experiments. The group meetings where each graduate student rotated to present their work also provided a pleasant forum for discussing research. Over the years, my research work evolved into studying optical vortices, and this dissertation write-up is focused on one of the problems studied.

I also benefited from interacting with my dissertation committee members: Paul Berman, Tal Carmon, Georg Raithel, and Steve Rand. In Paul Berman's class on quantum optics, the homework contained a series of challenging problems that I still sometimes think about. It was especially pleasurable meeting with Paul to discuss my research, and gain insight as to its importance to the scientific community. Tal Carmon has an uncanny way of doing research, and the questions he often posed always challenged me to think even harder and more carefully about my research problem; more importantly, how new and interesting research work can be extracted from it. One of the highlights of my graduate career was volunteering in the physics Olympiad for high school students which Georg organizes annually. I have also stopped by

Georg's office from time to time to discuss my research, and get a sense of interesting and innovative applications of my research work. During my later years of graduate school, Steve Rand's critique challenged me to think of alternative ways of presenting the work in this dissertation.

I would also like to acknowledge mentors who have been there at various times of need at the University of Michigan: Roy Clarke, Alec Gallimore, Duncan Steel, Cagliyan Kurdak, and Brad Orr. I met many of these faculty members during my visit to Michigan, and have interacted with them throughout graduate school to discuss my progress in the research program, and how to successfully advance to the next level. They have always been very warm and welcoming, with great optimism about the future. It was also delightful to discuss my research work with them and volunteer with Roy during the physics Olympiad.

I would like to acknowledge my past research mentors: Claire Gmachl (Princeton University), Gregory Boutis (CUNY), Farley Mawyer (CUNY), Martin Culpepper (MIT), and Chris Monroe (University of Maryland), as well as many members of their research teams whom I became acquainted with and learned from. Through my undergraduate mentors, I was exposed to the research community on a number of different levels and gained valuable insight on the general principles to follow to become a successful researcher. They also provided me with opportunities and advice which I still use when contemplating my research work today. My graduate research began in Chris Monroe's ion trap group here at Michigan where I spent a year, from 2006-2007, and was initially exposed to experimental atomic physics and ion trapping principles. My experiences with these mentors in many ways set the stage for shaping my current methodology in thinking about and performing research.

I would like to acknowledge the AMO research group members: Emily Alden, Jeongwon Lee, Kaitlin Moore, Skyler Degenkolb, Chuck Siedlecki, Rabin Paudel, Charlie Steiner, Peter Tarle, Andrew Cadotte, and Jinhai Chen. These are people in

the lab whom I have spent time with in graduate school. Some of the questions which they raised have challenged me to think further about certain aspects of my research, which have sometimes yielded better solutions to existing problems, or just got me fantasizing about what may be possible with the available resources in the lab.

I would like to acknowledge the trapped ion quantum information research group: Dan Stick, Jon Sterk, Peter Maunz, Kathy-Anne Brickman, Dzmitry Matsukevich, Dave Moehring, Mark Acton, Simcha Korenblit, Kelly Younge, and Steve Olmschenk. These are people whom I interacted with significantly in lab during my first year of graduate school here at Michigan. In particular, I worked directly with Dan Stick and Jon Sterk, and benefited from discussions with various group members to better understand the experiment, which was undergoing major changes at the time, as well as learned the general principles behind ion trapping which transcends through much of atomic physics.

I would like to acknowledge friends who have constantly kept me sane in graduate school: Mitaire and Anette, Taey, Chuck, Ibou and Evgenia, Cyndi, Vasudev, Divine, Rashidah. In many ways, Mitaire and Anette have been family to me here in Michigan. Mitaire has a great sense of humor and excitement about life which is contagious. He has a way of keeping people around him upbeat, including me. The social get-togethers which he organizes are always wonderful, and I certainly appreciate the abundance of food prepared and packaged during some of my most stressful times in graduate school.

I would like to acknowledge my extended family whom I spent much of my childhood with: My late uncle Sode-Shinni Rumala (Baba Agie) who instilled in me my love of math and science and the will to carry on regardless of the circumstance, my uncle John Saba, as well as my extended brothers and sisters who have been some of my biggest fans in many of my academic endeavors.

Without the support of my family I would not have reached the point I am today:

YaBodi, YaBaba and Yawo Dorothy, Zain, Adi, Aunty Diane, god father Ganiu Demu, Mom, and Dad. To my family, a big "Thank you". You have looked for possibilities to help me advance in ways that I could only imagine, but never thought possible. I was probably not the brightest in the family, but have have worked extremely hard over the years to complete a series of small tasks that generally leads up to big accomplishments. I was encouraged to apply for internships as an undergraduate student, and these experiences gave me a flavor of graduate school as well as some insight into how the research community works. I must admit, after all these years performing academic research that I am still learning the politics and inner workings of the academic and research community.

There are countless others (relatives, friends, acquaintances, academic faculty members, ...etc) who have supported me in my journey through graduate school, and life in general, who are not mentioned in this acknowledgment. A big thank you! I appreciate the support.

I had the opportunity to be awarded a number of fellowships for my graduate studies: NSF Graduate Research Fellowship, Rackham Merit Fellowship and travel grants, Applied Physics Fellowship, and NSF sponsored AGEP mini-grants. The speed at which many research projects were executed would not have been possible without generous funding from these sources which have either provided stipends to minimize distractions when doing research, or provided travel support to conferences to broaden my network.

# TABLE OF CONTENTS

# LIST OF FIGURES

**Figure**

# LIST OF APPENDICES

**Appendix**

# ABSTRACT

A new etalon geometry: The spiral phase plate etalon

by

Yisa S. Rumala

Chair: Aaron E. Leanhardt

This dissertation reports on theory, simulations, and experiments that extend the conventional Fabry-Perot etalon to a new geometry, namely the spiral phase plate etalon. In the development of the theory, the spiral phase plate etalon is treated in the thin plate approximation and thick plate approximation. The thin plate approximation elucidates properties of the device such as the presence of a coherent superposition of orbital angular momentum modes with different winding numbers in the device, and an intensity pattern that varies as a function of angle. The thick plate approximation captures additional angular interference phenomena in the high finesse limit of the device not seen in the thin plate approximation. These are distinguishing features of the spiral phase plate etalon compared to the conventional Fabry-Perot etalon, which is treated for the first time in this dissertation.

In the experiment, optical transmission through the spiral phase plate etalon is probed with a laser beam, and observed to have an intensity variation as a function of angle. The angular intensity pattern is observed to rotate when the laser frequency is varied. These properties of the spiral phase plate etalon are measured and experimentally quantified for the first time. The experimental data is compared to theory, and

simulations of the optical intensity profiles in which the dominant source of noise is shot noise. In each case, the statistical uncertainty of the parameters used to describe the spiral phase plate etalon are determined, for which the phase sensitivity of the angular intensity pattern to rotation is deduced. The simulations are also used to understand systematic errors in the data.

In addition, the optimal parameters to design a spiral phase plate etalon for best position and frequency resolution (sensitivity) of the optical angular intensity pattern to rotation is obtained. This device is expected to have wide ranging applications, including the possibility to serve as a unique tool in optical frequency metrology, as well as in the study of atomic and molecular physics, quantum optics and quantum information science.

# CHAPTER I

# Introduction

In 1897, Charles Fabry and Alfred Perot reported on the invention of an interferometer consisting of two perfectly flat glass plates which can be mechanically varied (1). This interferometer produced remarkable interference fringes. When the same principle is applied to a single transparent plate with reflecting surfaces as opposed to two reflecting glass plates, the device is called a Fabry-Perot etalon. A property of the Fabry-Perot etalon is that it has longitudinal modes in the direction of beam propagation. In this dissertation, a novel geometry of the etalon is studied in detail, namely the spiral phase plate etalon. In this case, one surface is flat, and the other surface has an azimuthally varying height. As light propagates through the device, it creates interference fringes as a function of azimuthal angle, in addition to the longitudinal modes in the device. The reason for the beam having angular interference fringes as a function of angle is because the device contains a coherent superposition of orbital angular momentum modes on the output plane of the device. This is a distinguishing feature of the spiral phase plate etalon compared to the conventional Fabry-Perot etalon, and it is further discussed in chapter II of this dissertation.

The angular momentum carried by light can have distinct spin (2; 3) and orbital (4; 5; 6; 7) contributions, which originate from the polarization and spatial structure of the electromagnetic field associated with light, respectively. The spin angular

momentum is associated with circular polarization, and can take on values of either $+\hbar$ or $-\hbar$ indicating right or left circularly polarized light, respectively. The orbital angular momentum of light is independent of light's polarization state, and can take on any positive or negative integer value of $\hbar$. In recent years, there have been many new and exciting applications of laser beams containing orbital angular momentum in quantum information science (8; 9; 10; 11; 12; 13; 14; 15; 16; 17; 18; 19; 20; 21; 22; 23), atom optics (24; 25; 26; 27; 28; 29; 30; 31), and optical tweezer experiments (32; 33; 34; 35; 36).

Light beams with orbital angular momentum, i.e. optical vortices, has rich structure, and have been produced via mode competition in laser cavities (37; 38), diffraction from holograms (39; 40; 41; 42), propagation through cylindrical lens mode converters (43; 44; 45), and transmission through spiral phase plates (46; 47; 48). While all these methods have been used to create optical vortices with great success, the spiral phase plate, which was first demonstrated in 1994 (48), provides the simplest and most intuitive explanation as to how a beam with uniform transverse phase acquires orbital angular momentum as it propagates through the device.

An ideal spiral phase plate consists of a transparent material with uniform refractive index and an azimuthally varying thickness such that as light goes through the material it acquires an azimuthally varying phase corresponding to a winding number. The winding number can be defined as the number of intertwined wavefronts in the beam, and is a direct measure of the orbital angular momentum of light. In all work up to now, transmission through a spiral phase plate has been treated in the context of a device with zero reflectivity on both surfaces where a laser beam propagates through the phase plate and acquires a winding number which depends on the azimuthally varying thickness, wavelength, and refractive index of the spiral phase plate. Due to diffraction, the intensity profile of the beam has a ring (or donut) structure millions of light wavelengths far away from the device (diffraction far field),

and a Gaussian structure within a few wavelengths of the device (diffraction near field).

In this dissertation, I present the first detailed studies of a device with non-zero reflectivity on both surfaces, i.e. a spiral phase plate etalon. As the beam propagates through the device, the beam will make multiple round trips before exiting the device. Each time the beam makes a round trip, it will acquire an additional azimuthally varying phase. The sum of all the different phases will interfere constructively and destructively to create intensity maxima and minima as a function of angle. This work forms a new etalon geometry, and extends the operation of the conventional Fabry-Perot etalon consisting of longitudinal modes, to include angular interference fringes on the output plane of the device. As the conventional Fabry-Perot etalon has been the work horse in many experiments involving precision frequency metrology, the spiral phase plate etalon is expected to have applications in this area as well. Furthermore, since the beam coming out of the spiral phase plate etalon also possess orbital angular momentum, unlike the conventional Fabry-Perot etalon, it is expected to have even broader applications in quantum information science, atom optics and optical tweezer experiments. It may be especially advantageous in new experiments that explore coherent control of atoms, molecules and solid state systems. Specific examples are discussed in chapters V and VI of this dissertation.

From a quantum optics perspective, an intriguing and fascinating feature of the spiral phase plate etalon is that it contains a coherent superposition of optical vortices with different winding numbers, i.e. different orbital angular momentum modes of the field. In addition, the optical intensity profiles presented in this dissertation does not have a large vortex core (and in some cases both a large vortex core and large azimuthal region with zero intensity) that appears in previous studies (10; 11; 12; 19; 49; 50; 51; 52; 53). This is because the optical intensity profile is imaged immediately after the spiral phase plate etalon. The spiral phase plate etalon represents a unique

geometry to generate these orbital angular momentum states as well as manipulate these states by changing the frequency of light propagating through the device.

## 1.1 Overview of dissertation

This dissertation is written in manuscript form, and therefore the content in some of the chapters may overlap.

- In chapter II, the theory of multiple beam interference in a spiral phase etalon is developed. In particular, the theory is developed in the context of the thin plate approximation and thick plate approximation, and the implications of both approximations are discussed.

- Chapter III describes the optimal design parameters to fabricate a spiral phase plate etalon for best position and frequency resolution (sensitivity) to rotation of an optical angular interference pattern on the output plane of the device. In addition, the chapter reports on tools to analyze the computer generated optical intensity profile emerging from an ultra-low finesse spiral phase plate etalon (i.e. a finesse of $\sim 1$).

- In chapter IV, measurement of multiple beam interference effects in a spiral phase plate etalon is reported, and the results are compared to theory and simulation. Noise and error sources in the experiment which may limit the sensitivity of the etalon are discussed.

- In chapter V, the rotation of the optical angular interference pattern as a function of laser frequency is experimentally quantified and compared to theory and simulations.

- The dissertation concludes with chapter VI, where some of the exciting possibilities of the spiral phase plate etalon as a useful tool in applied and fundamental

research are discussed.

- The appendix contains additional calculations and discussions to complement the work presented in the chapters.

# CHAPTER II

# Theory of multiple beam interference in a spiral phase plate

## 2.1 Introduction

In this chapter, optical transmission through a spiral phase plate is calculated for a realistic device with nonzero reflectivity at both of its surfaces. The spiral phase plate is modeled as a Fabry-Perot etalon with a pair of parallel, planar surfaces that are separated by an azimuthally-varying distance. This is referred to as the thin plate approximation. Multiple reflections within the device produce a transmitted beam comprising of a coherent superposition optical vortices with different winding numbers. Interference between the different optical vortex modes imprints a periodic, azimuthal modulation onto the intensity profile. In addition, the average distance and average lifetime of the photon counts in the spiral phase plate is estimated. Towards the end of this chapter, the spiral phase plate in the thick plate approximation is treated where one surface is assumed to be perfectly flat and the other surface has an azimuthally varying height as opposed to parallel and planar surfaces.

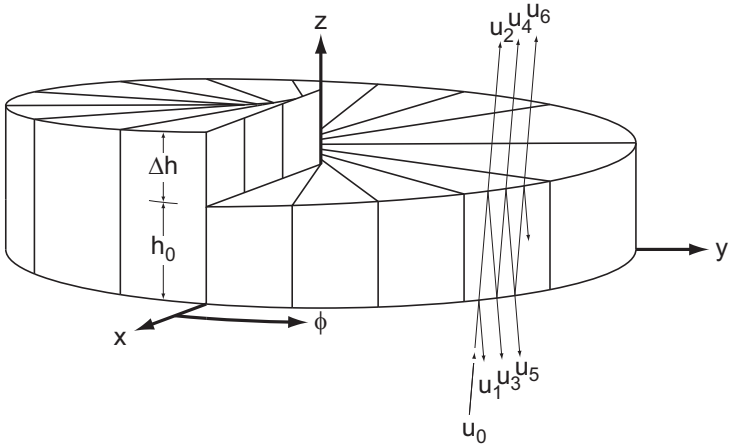


Figure 2.1: Multiple-beam interference. Approximating a spiral phase plate as a Fabry-Perot etalon with an azimuthally varying thickness $h(\phi)$ yields reflected, $u_R = u_1 + u_3 + u_5 + \cdots$, and transmitted, $u_T = u_2 + u_4 + u_6 + \cdots$, waves that contain a coherent superposition of optical vortices with different winding numbers.

## 2.2 Spiral phase plates in the thin plate approximation

Transmission through a spiral phase plate is analyzed in cylindrical polar coordinates for an incident electromagnetic wave propagating in the $+\hat{z}$ direction with a time-dependent electric field vector $\vec{E}(r, \phi, z, t) \propto \Re e\{u(r, \phi, z)e^{-i\omega t}\hat{\varepsilon}\}$, where $u(r, \phi, z)$, $\hat{\varepsilon}$, and $\omega$ are the complex-valued amplitude, unit polarization vector, and angular frequency of the wave, respectively. An ideal spiral phase plate comprises a medium of refractive index $n$ with an azimuthally varying thickness (Fig. 2.1) (38; 48; 46):

$$h(\phi) = h_0 + \Delta h \frac{\phi}{2\pi} \quad (0 \leq \phi \leq 2\pi). \tag{2.1}$$

It is assumed that the incoming beam hits the input plane of the spiral phase plate at normal incidence and that the device is surrounded by vacuum ($n = 1$).

Typically, optical transmission through a spiral phase plate is analyzed using the thin plate approximation within scalar diffraction theory (57; 58; 59; 60) such that the wave amplitudes at the input ($z = 0$) and output ($z = h_0 + \Delta h$) planes of the

device are related by (64):

$$t_{\text{thin}}(\phi) = \frac{u(r,\phi,h_0+\Delta h)}{u(r,\phi,0)} = t_0 e^{+i\alpha\phi}, \tag{2.2}$$

where $t_0 = e^{+inkh_0}e^{+ik\Delta h}$, $\alpha = (n-1)\frac{\Delta h}{\lambda}$ is the 'winding number' or 'charge' of the spiral phase plate, and $k = \frac{2\pi}{\lambda}$ is the vacuum wavevector of the light with vacuum wavelength $\lambda$. The intensities, $I(r,\phi,z) \propto |u(r,\phi,z)|^2$, at the input and output planes of the device are identical because $|t_{\text{thin}}(\phi)|^2 = 1$.

The derivation of Eq. 2.2 assumes zero reflectivity from both surfaces of the spiral phase plate. A realistic spiral phase plate can be approximated as a Fabry-Perot etalon with an azimuthally varying thickness, i.e. a medium of refractive index $n$ with *parallel* surfaces separated by a position-dependent distance $h(\phi)$ (Eq. 2.1). It has been assumed that the absorption by the material is zero. The complex-valued amplitude transmittance function for the spiral phase plate then becomes

$$t_{\text{thin}}(\phi) = \frac{u(r,\phi,h_0+\Delta h)}{u(r,\phi,0)} \tag{2.3a}$$

$$= t_2 t_1 t_0 e^{+i\alpha\phi} \sum_{m=0}^{\infty} \left(r_2^2 e^{i\beta(\phi+\phi_0)}\right)^m \tag{2.3b}$$

$$= \frac{t_2 t_1 t_0 e^{+i\alpha\phi}}{1 - r_2^2 e^{+i\beta(\phi+\phi_0)}} \tag{2.3c}$$

where $\beta = 2n\frac{\Delta h}{\lambda}$, $\phi_0 = 2\pi\frac{h_0}{\Delta h}$, and the Fresnel reflection and transmission coefficients (58; 57) applicable for rays crossing from vacuum into the medium of refractive index $n$ and for rays crossing from the medium of refractive index $n$ into vacuum are $\{r_1 = \frac{1-n}{n+1},\ t_1 = \frac{2}{n+1}\}$ and $\{r_2 = \frac{n-1}{n+1},\ t_2 = \frac{2n}{n+1}\}$, respectively. The intensities at the input and output planes of the device now have different profiles. Specifically,

$I(r, \phi, h_0 + \Delta h) = |t_{\text{thin}}(\phi)|^2 I(r, \phi, 0)$ with

$$|t_{\text{thin}}(\phi)|^2 = \frac{1}{1 + \frac{4|r_2|^2}{(1-|r_2|^2)^2} \sin^2\left(\frac{\beta(\phi+\phi_0)}{2}\right)}, \tag{2.4}$$

which has a periodic modulation as a function of azimuthal angle, $\beta$. Physically speaking, $\beta$ also determines the number of peaks in the angular interference pattern, and the orbital angular momentum states present in the spiral phase plate, which is described in the next section. $r_2$ determines the modulation amplitude and the single fringe width of the etalon, and $\phi_0$ determines the position of the angular interference fringes. An alternative method for calculating Eq. 2.3 is in Appendix B. Since it been established that the device is an etalon with a flat surface on one end and an azimuthally varying surface on the other end, the device can be referred to as a "spiral phase plate etalon". For much of this dissertation, the term "spiral phase plate etalon" and "spiral phase plate" will be used interchangeably.

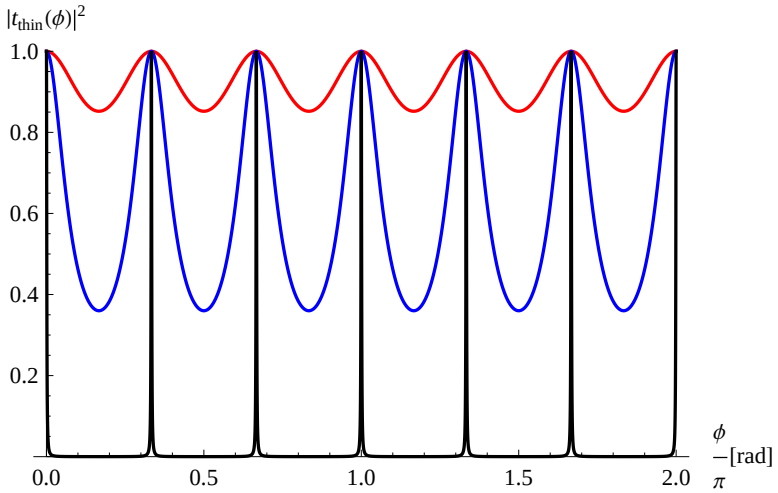


Figure 2.2: Transmission through an etalon for a hypothetical value of $\beta = 6$ and Fresnel reflectivity of $r_2 = 0.2$ (red), $r_2 = 0.5$ (blue) and $r_2 = 0.99$ (black). The value of $\beta$ gives the number of transmission peaks in a $2\pi$ rad azimuthal angle. The value of $\beta$ also determines the orbital angular momentum states present in the spiral phase plate as described in the next section (section 2.2.1).

### 2.2.1 Orbital angular momentum states in spiral phase plate

Precise control of the orbital angular momentum states in a spiral phase plate may be of significance in experiments involving quantum information and networking applications such as the ones in ref. (10) and ref. (12). This subsection describes the states present in the etalon and a few implications of treating the spiral phase plate as a Fabry-Perot etalon with an azimuthally varying thickness.

Quantum mechanics requires that the orbital angular momentum of a photon is quantized in integer multiples of $\hbar$ (65; 66). In particular, by calculating the overlap integral (67; 68; 69) of the spiral phase plate transmission function $t_{thin}(\phi)$ with the wave function, $e^{-i\ell\phi}$, the probability of detecting a "photon" with orbital angular momentum having projection $\ell\hbar$, $\ell = 0, \pm1, \pm2, \ldots$, along the z–axis is:

$$p_\ell = \frac{1}{N_\ell}\left|\int_0^{2\pi} t_{thin}(\phi)e^{-i\ell\phi}d\phi\right|^2 \tag{2.5a}$$

$$= \frac{1}{N_\ell}\left|\int_0^{2\pi} t_2t_1t_0e^{i\alpha\phi}\sum_{m=0}^{\infty}\left(r_2^{2m}e^{+i\beta m(\phi+\phi_0)}\right)e^{-i\ell\phi}d\phi\right|^2 \tag{2.5b}$$

$$= \frac{1}{N_\ell}\left(\left|t_2t_1t_0\right|^2\left|r^{2m}\right|^2\right). \tag{2.5c}$$

$N_\ell$ is a normalization factor which is $N_\ell = \left|t_2t_1t_0\right|^2\sum_{m=0}^{\infty}\left|r^{2m}\right|^2 = \left|t_2t_1t_0\right|^2\frac{1}{1-r_2^4}$. For a beam without orbital angular momentum incident on a spiral phase plate etalon fabricated with integer values of $\alpha$ and $\beta$, the transmitted beam contains "photons" having $\ell = \alpha + m\beta$, m=0,1,2,... with detection probabilities

$$p_m = (1 - |r_2|^4)|r_2|^{4m}. \tag{2.6}$$

For non-integer $\alpha$ and/or $\beta$, the transmitted electromagnetic field is frequently said to contain "fractional vortices". For the remainder of this dissertation, the term

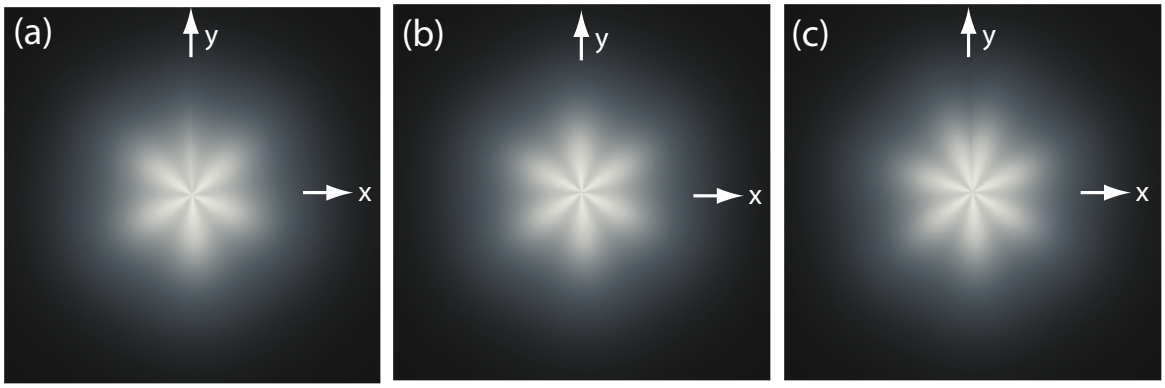


Figure 2.3: Calculated intensity profile of optical vortex on the output plane of the device (diffraction near field) in the thin plate approximation for (a) non-integer vortex of $\alpha = 0.99$ and $\beta = 5.55$, (b) integer vortex of $\alpha = 1$ and $\beta = 6.0$, and (c) non-integer vortex of $\alpha = 1.16$ and $\beta = 6.5$. The value of $\beta$ determines the number of intensity peaks in the angular intensity profile. The reflectivity on both surfaces of the spiral phase plate is $r_2 = 0.2$.

"fractional vortex" and "non-integer vortex" will be used interchangeably. Fig. 2.3 shows 2D intensity profiles immediately after the spiral phase plate etalon (diffraction near field) for non-integer and integer optical vortices. The diffraction far field for non-integer vortices are analyzed in refs. (10; 11; 12; 19; 49; 50; 51).

The implications of treating a spiral phase plate as a Fabry-Perot etalon with an azimuthally varying thickness are summarized for a hypothetical charge–1 device, e.g. a device with $n = 1.5$ and $\Delta h = 2\lambda$ yielding $r_2 = 0.2$, $\alpha = 1$, and $\beta = 6$. The optical intensity profile immediately after such a spiral phase plate etalon would have an angular modulation with peak-to-peak variation of $\sim 15\%$ and period of $\Delta\phi = \frac{\pi}{3}$. The transmitted beam would contain "photons" with $\ell = 1, 7, 13, 19, \ldots$, [Fig. 2.4] even though the probability of detecting "photons" in the transmitted beam having $\ell \neq 1$ would be only $p_{\ell \neq 1} = 0.0016$. This indicates that there is a large azimuthally varying modulation amplitude while less than 1% of the "photons" are projected into higher orbital angular momentum states. As seen in the plot of Fig. 2.2, and measured in chapter IV, these are measureable effects which may have to be taken

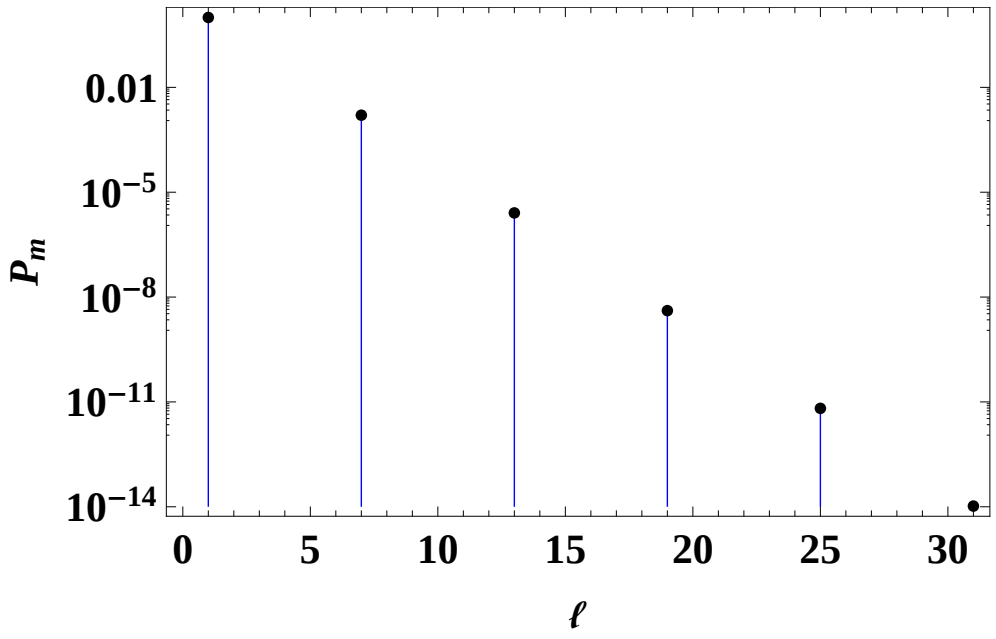


Figure 2.4: Probability of detecting photons in the distribution with winding number, $\ell = 1, 7, 13, 19, \ldots$. The transmitted optical beam through the spiral phase plate etalon is an infinite superposition of optical vortices with winding number $\ell$ spaced by a parameter quantifying the relative phase, $\beta = 6$. Even though m extends to infinity, only $0 \leq m \leq 5$ is shown in this figure.

into account when conducting quantum entanglement and correlation experiments with spiral phase plates such as the ones in ref. (10) and ref. (12).

The Fabry-Perot etalon effects can be reduced (enhanced) by decreasing (increasing) the reflectivity at the surfaces of the spiral phase plate, e.g. by adding dielectric or metallic coatings directly to the surfaces of the device. However, the derivation of Eq. 2.3 is not equivalent to placing an ideal spiral phase plate described by Eq. 2.2 between two parallel mirrors with amplitude reflectivity $r_2$. In that case, the transmitted beam would contain "photons" having $\ell = (2m + 1)\alpha$, $m = 0, 1, 2, \ldots$ with detection probabilities, $p_m$, still given by Eq. 2.6.

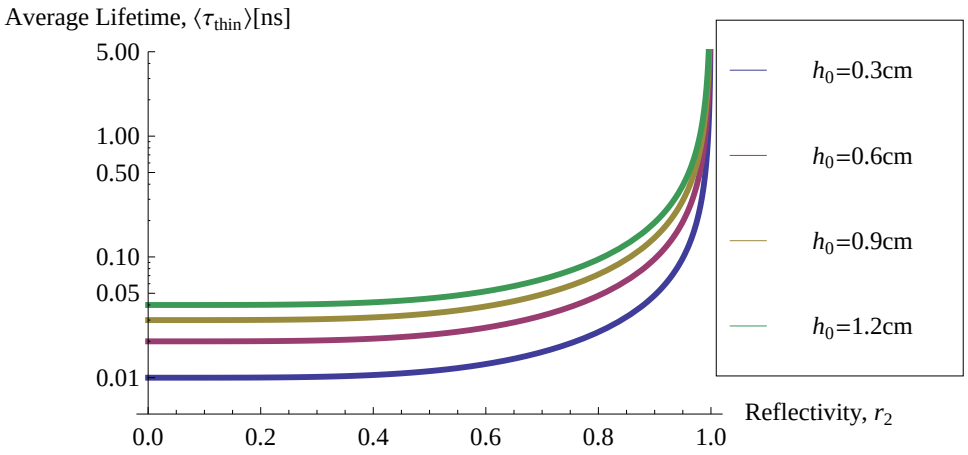


Figure 2.5: Average lifetime of the beam in the spiral phase plate etalon calculated in the thin plate approximation for different etalon base heights

### 2.2.2 Average distance and lifetime in the thin plate approximation

The average distance traveled by the beam in the the spiral phase plate etalon is

$$\langle d_{thin} \rangle = \frac{1}{N_d} \left( z + 3z(r_2^2)^2 + 5z(r_2^2)^4 + 7z(r_2^2)^6 + ... \right) \tag{2.7a}$$

$$= \left( \frac{r_2^4 + 1}{1 - r_2^4} \right) z|_{z=h_0} \tag{2.7b}$$

$N_d = N_l$ is a normalization constant derived in the previous section, and $h_0$ is the thickness (or base height) of the spiral phase plate etalon. The average lifetime of the device in the thin plate approximation is $\langle \tau_{thin} \rangle = \frac{\langle d_{thin} \rangle}{c}$, and it is illustrated in Fig.2.5 for different base heights. The lifetime is of significance when using the device for frequency metrology applications. The topic is further discussed in chapters III.

## 2.3 Spiral phase plates in the thick plate approximation

As seen earlier in this chapter, the thin plate approximation assumes that the two surfaces of the spiral phase plate etalon are parallel to each other and physical effects due to the azimuthally varying thickness on one surface is neglected i.e. the rays do not bend as it propagates from one refractive index to another. For a realistic device, these physical effects become important as the beam makes multiple bounces (i.e. high finesse etalon) and it leads to additional observable interference effects not captured by approximations in the thin plate approximation. Taking these physical effects into account will ultimately affect the design of the spiral phase plate for the desired application. A potential application where this may be important is in precision optical metrology such as designing new laser locking, and frequency stabilization systems which depends on measuring the position of the optical angular interference pattern accurately, as well as in more fundamental studies such as the evolution of dynamic (or possibly geometric) phases in the device due to changes in light frequency, refractive index, and/or azimuthal step height of the device.

In this section a calculation is performed in the thick plate approximation where the effect of the azimuthally varying surface is included. It is seen that the results for the thick plate approximation are much more complex compared to the thin plate approximation. Strictly speaking, a numeric model of propagation through the phase plate is required to fully understand problem. The analytic treatment presented here calculates the electric field amplitude at a single point of the azimuthally varying surface.

### 2.3.1 Transmission function in thick plate approximation

In the thick plate approximation, the device is modeled as a triangular wedge were the azimuthally varying surface makes an angle $\gamma$ with the flat surface as seen in Fig 2.6. $\Delta h$ is the step height, $h_0$ is the base height (or phase plate thickness) and $2\pi\omega_0$

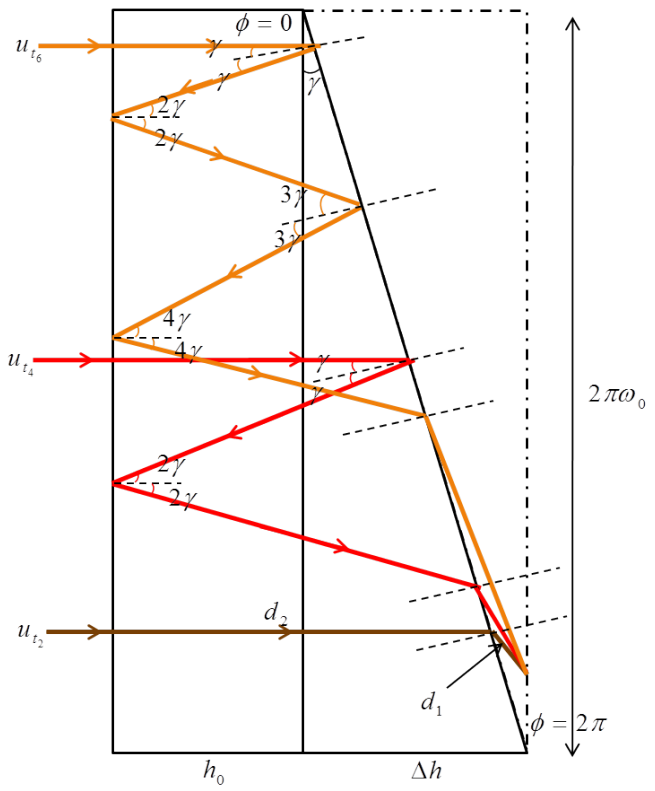


Figure 2.6: Angular wedge to model transmission function in the thick plate approximation. The azimuthal step height goes from 0 to $2\pi$ over a $2\pi\omega_0$ circumference of the input optical beam. $\omega_0$ is the beam waist. The transmitted beam is a superposition of electric field amplitudes, $u_{thick}(r, \phi, h_0 + \Delta h) = u_{t_2} + u_{t_4} + u_{t_6} + ....$ The field is calculated at a point where the light rays $u_{t_2}$, $u_{t_4}$, $u_{t_6}$ meet at a point on a uniform output plane.

is the circumference of the laser beam which goes from $\phi = 0$ to $\phi = 2\pi$. A triangular wedge to model the spiral phase plate etalon is expected to be valid for small angle between the azimuthal surface and flat surface such that $\tan\gamma = \frac{\Delta h}{2\pi\omega_0} \approx \gamma << 1$, where the spiral phase plate step height $\Delta h$ is on order the wavelength of light, $\lambda$.

The electric field is calculated by tracing the ray as it makes multiple reflections within the device. The transmission function is a superposition of the electric field amplitudes $t_{thick}(\phi) = u_{t_2} + u_{t_4} + u_{t_6} + ...$ at a point on the output plane as shown in Fig 2.6. Note that the transmission function is calculated on a uniform output plane, i.e. a point on the dashed line where all the light rays meet (See fig 2.6). A

property of the angular wedge is that during each successive bounce in the etalon, the angle of the beam increases by a value of $\gamma$. The small angle approximation is made throughout this calculation, where $\sin\theta \approx \theta$ and $\cos\theta \approx 1 - \frac{\theta^2}{2!}$, and Snell's law is used whenever the rays undergo a change in refractive index. The electric field amplitude for the first ray which makes no bounce in the etalon will be

$$u_{t_2} = t_1 t_2 e^{ikd_1} e^{inkd_2} \tag{2.8}$$

For conciseness, $d_1 = (\Delta h - \Delta h \frac{\phi}{2\pi})(1 + \frac{(n\gamma-\gamma)^2}{2})$ is the distance that the ray travels in vacuum between the azimuthally varying height and uniform output plane; and $d_2 = h_0 + \Delta h \frac{\phi}{2\pi}$ is the distance that the ray travels in the spiral phase plate. All other terms have their usual meanings as seen earlier in this chapter.

$$u_{t_4} = t_1 t_2 r_2^2 e^{ikd_1(1+4(n\gamma)^2)} e^{inkd_2(3-4\gamma^2)} e^{-ink6n\gamma^2 \frac{d_1}{1+(\frac{(n\gamma-\gamma)^2}{2!})}} \qquad \text{2 bounces} \tag{2.9a}$$

$$u_{t_6} = t_1 t_2 r_2^4 e^{ikd_1(1+12(n\gamma)^2)} e^{inkd_2(5-20\gamma^2)} e^{-ink20n\gamma^2 \frac{d_1}{1+(\frac{(n\gamma-\gamma)^2}{2!})}} \qquad \text{4 bounces} \tag{2.9b}$$

$$u_{t_8} = t_1 t_2 r_2^6 e^{ikd_1(1+24(n\gamma)^2)} e^{inkd_2(7-56\gamma^2)} e^{-ink42n\gamma^2 \frac{d_1}{1+(\frac{(n\gamma-\gamma)^2}{2!})}} \qquad \text{6 bounces} \tag{2.9c}$$

The complex valued transmittance function of the electric field amplitude in the thick plate approximation then becomes:

$$t_{thick}(\phi) = \frac{u_{thick}(r,\phi,h_0+\Delta h)}{u_{thick}(r,\phi,0)} = u_{t_2} + u_{t_4} + u_{t_6} + ... \tag{2.10a}$$

$$= t_1 t_2 e^{ikd_1} e^{inkd_2} \sum_{m=0}^{m=M} \left[ r^{2m} e^{ikd_1 2^2 m(n\gamma)^2} e^{inkd_2(2m - 2^2\gamma^2 \frac{2}{3} m(m+1)(2m+1))} \right] e^{-ik2M(2M+1)\frac{d_1}{1+\frac{(n\gamma-\gamma)^2}{2!}}} \tag{2.10b}$$

$$= t_1 t_2 e^{ik(\Delta h - \Delta h \frac{\phi}{2\pi})(1+\frac{(n\gamma-\gamma)^2}{2!})} e^{ink(h_0+\Delta h \frac{\phi}{2\pi})} \sum_{m=0}^{m=M} [r^{2m} e^{ik(\Delta h - \Delta h \frac{\phi}{2\pi})(1+\frac{(n\gamma-\gamma)^2}{2!})} 2^2 m(n\gamma)^2$$

$$e^{ink(h_0+\Delta h \frac{\phi}{2\pi})(2m-2^2\gamma^2 \frac{2}{3} m(m+1)(2m+1))}] e^{-ik2M(2M+1)n\gamma^2 \frac{(\Delta h - \Delta h \frac{\phi}{2\pi})(1+\frac{(n\gamma-\gamma)^2}{2!})}{1+\frac{(n\gamma-\gamma)^2}{2!}}} \quad (2.11)$$

When $\gamma = 0$, the transmission function satisfies the thin plate approximation, and Eq. 2.3 is reproduced. However, it is noticed that the transmission function does not form a geometric series as in the thin plate approximation. This is evident by the presence of nonlinear terms in m. The calculation presented in this subsection shares similarities with previous wedge models [e.g. ref. (61), (62), and (63)] in that during each successive reflection in the device, the angle increases by $\gamma$. However, the calculation differs from previous wedge calculations [e.g. ref. (61), (62) and (63)] in that Eq. 2.11 represents the amplitude transmission function coefficient of a superposition of electric field amplitudes at a single point on an azimuthally increasing surface of the output plane [dashed line of Fig. 2.6] of the device, and not a wedge of monotonically increasing height in the direction of beam propagation. In addition, beyond the output plane of the spiral phase plate etalon, the field distribution evolves into having a region of zero intensity in the middle of the intensity pattern, i.e. a vortex core, which gets larger as the beam propagates far away from the device, and so a calculation far away from the device will yield a different field amplitude. In order to fully understand the problem, a numeric model for propagation through the device is required.

In the ultra-low finesse regime (reflectivity $r_2 = 0.2178$ and finesse $F \sim 1$), the transmission functions in the thick plate and thin plate appears to yield similar results as shown in Fig. 2.7(a). The parameters used in generating the plots to check the agreement between the thin and thick plate approximation are $\lambda = 632.991nm$, $\Delta h = 1.129\mu m$, and $\frac{1}{e^2}$ beam radius of $\omega_0 = 1.48mm$, the reflectivity is $r_2 = \frac{n-1}{n+1} = 0.217$, $\beta = 2n\frac{\Delta h}{\lambda} = 5.55$ and $\gamma = \frac{\Delta h}{2\pi\omega_0} = 1.21 \times 10^{-4}$rad. In principle, since $\gamma << 1$,

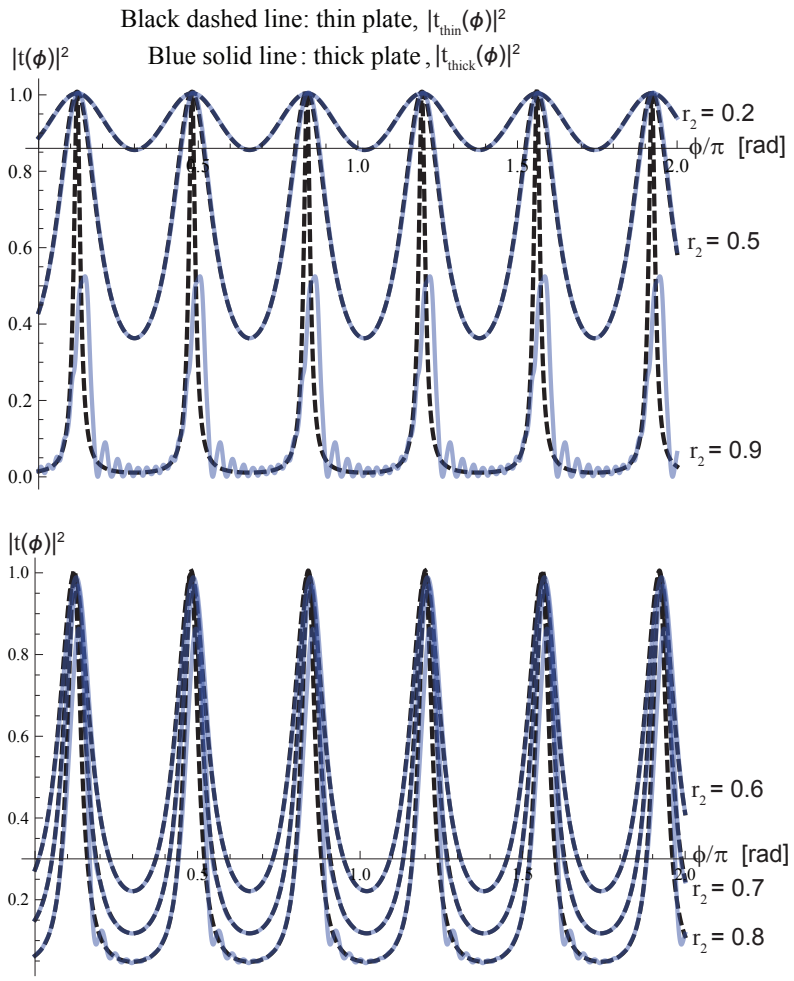


Figure 2.7: (a) Transmission function with peak intensity thin (modulus square of Eq. 2.3, Black dashed line) and thick plate (modulus square of Eq. 2.11, Solid blue) approximation for a spiral phase plate of $\beta = 5.55$ and $\gamma = 1.21 \times 10^{-4}$rad. The thin and thick plate approximation appears to yield similar results for low values of reflectivity, i.e. $r_2 = 0.2$ and $r_2 = 0.5$. However, for high reflectivity, i.e. $r_2 = 0.9$, there appears to be additional interference phenomenon captured in the thick plate approximation calculation, but not in the thin plate approximation calculation. The width of the fringe for $r_2 = 0.9$ also appear to be wider in the thick plate approximation calculation compared to the thin plate approximation calculation. The peak intensity for $r_2 = 0.9$ also reduces by approximately a factor of two in the thick plate approximation compared to the thin plate approximation. (b) Transmission intensity peaks for intermediate reflectivity values, i.e. $r_2 = 0.6$, $r_2 = 0.7$, and $r_2 = 0.8$. In these plots, the point at which the thick plate approximation starts to deviate from the thin plate approximation is around $r_2 = 0.7$. This is characterized by smaller peak heights and then at even higher reflectivity ($r_2 = 0.8$) there are additional fringes at the base of the main interference peaks.

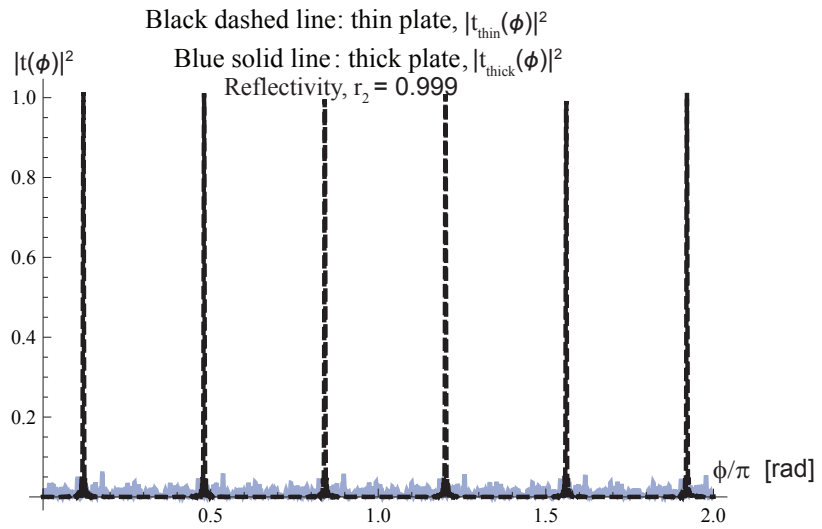


Figure 2.8: The transmission peak intensity is normalized to 1 in the thin plate approximation. When $r_2 = 0.999$, the interference fringes in the thick plate (modulus square of Eq. 2.11, Solid blue) approximation is no more visible compared to the thin plate approximation (modulus square of Eq. 2.3, Black dashed line), for a spiral phase plate of $\beta = 5.55$, and $\gamma = 1.21 \times 10^{-4}$rad.

this validates the initial approximation in the thin plate approximation regarding the etalon surfaces being parallel for an ultra-low finesse etalon ($r_2 = 0.2$). Most of the theory and experimental measurements in future chapters is described in the context of the thin plate approximation since an ultra-low finesse etalon is used in the experiments.

The calculations in the thin plate approximation are no more valid at the point were the thin and thick plate approximation starts to yield different results. For a wavelength of $\lambda = 632.991nm$, azimuthal step height of $\Delta h = 1.129\mu m$ and a phase plate base height of $h_0 = 0.6cm$, the thin and thick plate approximation appear to yield similar results up until approximately $r_2 = 0.7$, after which noticeable changes between the two approximations starts to emerge. These changes are characterized by the thick plate approximation calculations having a slightly smaller peak height and additional interference effects at the base of the transmission peaks compared to

the corresponding thin plate approximation calculations [see fig. 2.7(b)]. The peak of the interference fringes is also slightly shifted compared to the fringes in the thin plate case as calculated for $r_2 = 0.7$, $r_2 = 0.8$, and $r_2 = 0.9$ in Fig. 2.7.

At high reflectivity, i.e. $r_2 = 0.9$, the angular interference fringes appear to be narrower in the thin plate approximation than in the thick plate approximation and the additional interference effects captured in the thick plate approximation is clearly visible [see fig. 2.7(a)]. The peak intensity of the interference fringes at $r_2 = 0.9$ in the thick plate approximately is also approximately half the value in the thin plate approximation as seen in fig. 2.7(a). At an even higher reflectivity, i.e. $r_2 = 0.999$, the additional interference effects appear to be larger in magnitude compared to the angular interference fringes and much smaller (by about a factor of 15) compared to the transmission peaks in the thin plate approximation [See fig. 2.8]. In addition, there are no well resolved angular fringes corresponding to an angular modulation of $\beta = 5.55$ for an $r_2 = 0.999$ spiral phase plate etalon in the thick plate approximation.

### 2.3.2 Beam walk around distance in spiral phase plate due to multiple reflections

In a realistic spiral phase plate, the two surfaces are not parallel to each other. Hence, as the beam makes multiple bounces in the spiral phase plate, the successive rays exit at larger angles and travel in the direction of increasing azimuthal thickness. As it is the field amplitude that makes multiple reflections with the azimuthally increasing thickness that are in the higher orbital angular momentum modes, this suggest that these field amplitudes should exit the device in such a way that it is bent towards the direction of increasing azimuthal thickness from a ray optics perspective (See fig. 2.9). The azimuthal distance traveled over a $2\pi$ radian angle before the beam makes another azimuthal round trip or walks off the beam waist in the radial direction is calculated in this section (See fig. 2.9).

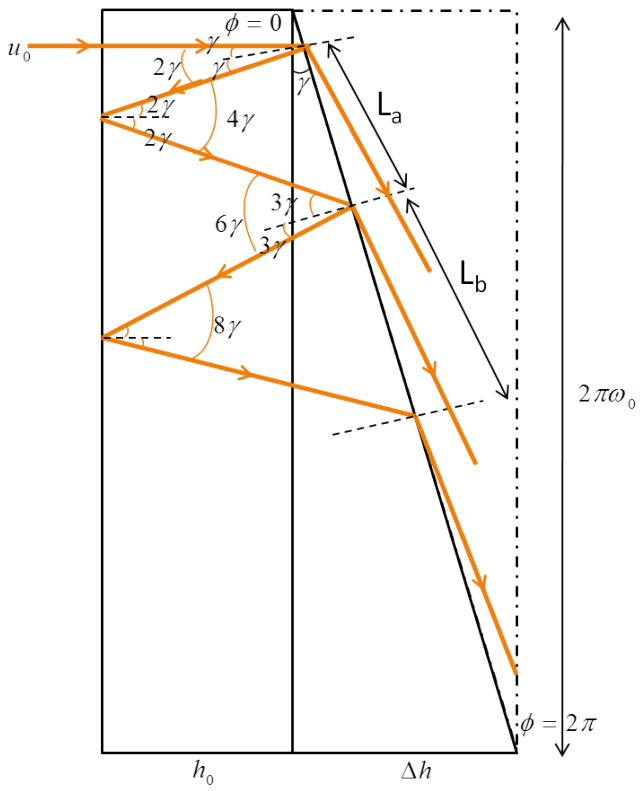


Figure 2.9: As the light rays makes multiple reflections with the azimuthally varying surface, it comes out at larger angles and is bent towards the direction of increasing thickness.

In the small angle approximation, the azimuthal distance traveled on the azimuthally varying surface after 2 reflections with the surface is $L_a = 4\gamma\left(h_0 + \Delta h\frac{\phi}{2\pi}\right)$ (See fig. 2.9). The azimuthal distance traveled after 3 reflections with the azimuthal surface is $L_b = 12\gamma\left(h_0 + \Delta h\frac{\phi}{2\pi}\right)$, and after 4 reflections is $L_c = 24\gamma\left(h_0 + \Delta h\frac{\phi}{2\pi}\right)$. Hence, the distance traveled on the azimuthal surface of the spiral phase plate etalon after $N+1$ $(N = 1, 2, 3, ...)$ reflections with the azimuthal surface is

$$L_{N+1} = \left(h_0 + \Delta h\frac{\phi}{2\pi}\right) 2N\left(N+1\right)\gamma \qquad N = 1, 2, 3, ... \tag{2.12}$$

Typically, the device is fabricated such that $h_0 >> \Delta h$, which gives rise to an az-

imuthal travel distance of

$$L_{N+1} = h_0 2N\,(N+1)\,\gamma \qquad \text{N=1, 2, 3,...} \tag{2.13}$$

As seen in Fig. 2.9, the total length of the spiral phase plate azimuthally varying surface for a beam waist, $\omega_0$, is $L_T = \sqrt{(2\pi\omega_0)^2 + \Delta h^2}$, and the angle between both surfaces is related to the step height and beam waist given by $\tan\gamma = \frac{\Delta h}{2\pi\omega_0}$. By setting $L_{N+1} = L_T$, and solving for N, a geometric factor describing the number of reflections that the beam makes with azimuthally increasing surface before it makes another azimuthal round trip or walks off the initial input beam waist in the radial direction can be obtained. For typical parameters such as $2\pi\omega_0 = 2\pi \times 1.1mm, h_0 = 6mm$, and $\Delta h = 1.8\mu m$, the beam makes 1.4 reflections with the azimuthally varying surface before making another $2\pi$ radian azimuthal travel distance in the etalon or walk off the initial input beam waist in the radial direction. It must be noted that the calculation in this subsection does not explicitly include the role which the reflectivity plays in determining the lifetime of photon counts in the etalon and hence the number of reflections with the azimuthally varying surface. This calculation instead puts a constraint on the number of reflections in the spiral phase plate etalon given the geometry of the device and the optical beam input parameters.

## 2.4 Concluding remarks

The theory of transmission through a spiral phase plate etalon has been discussed in the thin and thick plate approximation. In the limit of zero angle between the flat surface and the azimuthal surface, $\gamma = 0$, the thick plate approximation reproduces the thin plate approximation. The calculations in the thin plate approximation introduced a new phase factor not present in the current literature to describe the number of transmission peaks as a function of angle and position of the interference

peaks in a $2\pi$ radian angle. From this new phase factor, it is shown that the beam emerging from the device contains a coherent superposition of orbital angular momentum modes and is expected to be of significance in quantum optics and quantum information experiments.

The calculation in the thick plate limit showed additional properties of the spiral phase plate etalon. That is, when a ray model is used to compute transmission through the device, the rays are bent in the direction of increasing azimuthal thickness and exits the device at larger angles after successive reflections with the azimuthal surface. This suggests that the beam in the larger orbital angular modes (i.e. higher winding number) will exit at larger angles. In addition, the calculation in the thick plate approximation elucidates the presence of perturbations in the transmission function phase due to a non-zero angle between the azimuthal surface and flat surface. These perturbations leads to additional interference effects in the high finesse case not captured in the thin plate approximation. These perturbations may be of importance when studying the evolution of phases (e.g. dynamic phases or geometric phases) in the device which depends on the azimuthally increasing or decreasing step height.

As discussed in the chapter, understanding the device in the thin and thick plate limit will ultimately affect the design of the the spiral phase plate etalon for the desired application. For a low reflectivity device, the thin plate approximation describes the device very well, and for a high reflectivity device, the thick plate approximation is expected to better describe the device. In chapters III, IV, and V, the computational tools and experiments are developed in the context of using a very low reflectivity ($r_2 \sim 0.2$) device for optical metrology were the thin plate approximation is valid.

# CHAPTER III

# Computed optical beam intensity and sensitivity of spiral phase plate etalon

## 3.1 Introduction

A unique feature of the spiral phase plate etalon, unlike the conventional Fabry-Perot etalon, is that the angular interference pattern consisting of a coherent superposition of orbital angular momentum modes can be seen unambiguously at the same time, and in real time and space on the charge coupled device (CCD) detector screen. This is because the optical intensity profile has a modulation amplitude as a function of angle on the output plane of the spiral phase plate etalon. Thus, the photon counts within the modulation amplitude of the angular interference pattern as well as the width of the interference fringes will play a role in determining the minimum resolution of the optical angular interference pattern to rotation.

In this chapter, the optimal design parameters to fabricate a spiral phase plate etalon in which the optical angular interference pattern emerging from the device has the best position and frequency sensitivity to rotation is discussed. In addition, this chapter reports on simulations of the optical intensity profile to better understand the effects of shot noise in estimating the parameters to quantify the behavior of the spiral phase plate etalon. In the development of the simulations, analysis is performed

on computer generated data in which the only source of noise in the simulation is shot noise. This implies that other realistic sources of error or noise such as optical beam distortions as the beam propagates through the device is neglected. Optical beam distortions could result from spiral phase plate fabrication defects, or thin layers/residue which may have accumulated on the device. Other more subtle effects could be due to the mechanical effects induced by light on optical components such as material heating, and vibrations of the experimental set-up during measurements. The theory and simulations in this chapter is developed in the context of the thin plate approximation described in chapter II.

An outline of this chapter is as follows:

- The chapter starts with section 3.2, in which the standard error of the photon counts making position measurements on the CCD detector is estimated analytically for all reflectivity. This estimate provides insight into the optimal spiral phase plate design parameters to improve the sensitivity of the optical angular interference pattern to rotation. In this case the calculation does not include random fluctuations in photon count from pixel to pixel on the CCD detector due to shot noise.

- Section 3.3 describes simulations of optical transmission through the spiral phase plate, where the dominant source of noise is shot noise due to photodetection. The details in developing the program as it relates to extracting some of the relevant spiral phase plate parameters are discussed. It must be noted that the term "simulations" and "computer generated" optical intensity profile are used interchangeably through out this dissertation. Further more, in this section and for the remainder of this dissertation, the spiral phase plate is treated in the context of an ultra-low finesse device (i.e. a device with amplitude reflectivity of $r_2 = 0.217$, resulting in finesse of $F \sim 1$).

- Section 3.4 describes a method for estimating the statistical uncertainty due to shot noise, and describes how an error bar is assigned to each data point. This value will later be used to weight each data point when fitting the computer generated optical intensity profile to extract the parameters describing the optical angular interference pattern.

- Section 3.5 describes how to make the computer generated data more presentable by averaging out the statistical fluctuations of the photon counts due to shot noise. The same principle will be applied to the experimental data in the proceeding chapters to make it more presentable.

- In section 3.6, the shot noise limited parameters describing the spiral phase plate is estimated through a weighted fit of a single shot computer generated optical intensity pattern by minimizing $\chi^2$. These shot-noise limited parameters are compared to the input parameters used to generate the optical intensity profiles. Two different nonlinear minimization algorithms which provides the central value and corresponding error bars on the computer generated intensity profile is discussed. In this method, fluctuations in photon counts due to shot noise from pixel to pixel on the CCD detector is assumed, and this method is the most useful when quantifying the experimental data in the proceeding chapters. In addition, analysis on the rotation of computer generated (simulated) optical angular interference pattern is also quantified in the section. Another unique feature of the spiral phase plate etalon is that the optical angular interference pattern repeats itself at select laser frequencies, and is discussed in section 3.6.

- The chapter concludes with section 3.7.

## 3.2 Calculated sensitivity of spiral phase plate etalon from standard error

In this section, the etalon sensitivity is calculated from the transmission function assuming there is no pixel to pixel photon count fluctuation, i.e. all the photon counts making position measurements on the CCD detector are weighted equally. The estimates in this section will enable a determination of the optimal parameters to design the etalon in which the optical angular interference pattern will have the best sensitivity (resolution) to rotation. This resolution is calculated from the standard error,

$$\delta R_{min} = \frac{\delta\phi_{FW}}{\sqrt{N_p}}. \tag{3.1}$$

$\delta\phi_{FW}$ is the width of a single etalon fringe, and $N_p$ is the number of photon counts enclosed in the volume of the laser beam's angular intensity modulation making position measurements (See Fig. 3.1). The assumption is that a single fringe of the transmission function has $\frac{N_p}{\beta}$ photon counts making position measurements on the detector which forms a Gaussian distribution of width $\delta\phi_{FW}$. Therefore, the minimum resolution on $N_p$ measurements for $\beta$ fringes in a $2\pi$ radian angle will be $\frac{\delta\phi_{FW}}{\sqrt{\frac{N_p}{\beta}\beta}} = \frac{\delta\phi_{FW}}{\sqrt{N_p}}$ as seen in Eq. 3.1. As derived in chapter II, the analytic transmission function (atf) in the thin plate approximation is:

$$T_{\text{atf}} = \frac{1}{1 + \frac{4|r_2|^2}{(1-|r_2|^2)^2}\sin^2\left(\frac{\beta(\phi+\phi_0)}{2}\right)} \tag{3.2a}$$

$$= \frac{1}{1 + \left(\frac{2F}{\pi}\right)^2 \sin^2(\varphi_h)}. \tag{3.2b}$$

The etalon finesse is $F = \frac{\pi r_2}{1-r_2^2}$, and the maximums in the transmission function will occur at $\frac{\beta(\phi+\phi_0)}{2} = \pi$. Thus, a parameter describing the spacing of the etalon peaks is $\phi_F = \frac{2\pi}{\beta} - \phi_0$ where $\phi_0 \in \left[0, \frac{2\pi}{\beta}\right]$, and so the single fringe width of the transmission

function is approximated as

$$\delta\phi_{FW} = \frac{\phi_F}{F} = \left(\frac{2\pi}{\beta}\right)\frac{1-r_2^2}{\pi r_2} \tag{3.3}$$

$\delta\phi_{FW}$ decrease monotonically for increasing reflectivity [See Fig.3.2(a)]. A larger value of modulation frequency, $\beta$, corresponds to higher azimuthal step heights, which would result in an effectively smaller transmission function fringe width. The total number of photon counts making position measurements on the CCD detector, $N_p$, in Eq. 3.1, is calculated by numerically integrating the transmission function in a cylindrically symmetric coordinate system:

$$N_p\left[r_2,\beta\right] = \int_0^{2\pi}\int_0^{\omega_0} I\left[r\right]\left(T_{\mathrm{atf}}[r_2,\beta,\phi] - \left(1 - A_{mod}\left[r_2\right]\right)\right) r dr d\phi \tag{3.4}$$

$I\left[r\right] = I_0 e^{-\frac{2r^2}{\omega_0^2}}$ is the Gaussian laser beam spatial intensity distribution, $A_{mod}\left[r_2\right] = \frac{4r_2^2}{\left(1+r_2^2\right)^2}$ is the modulation amplitude of the optical angular interference pattern, and $T_{\mathrm{atf}}[r_2,\beta,\phi]$ is the spiral phase plate transmission function in the thin plate approximation. A plot of the number of photon counts in the etalon making position measurements on the CCD detector is in Fig. 3.2(b) with 1D, 2D, and 3D transmission function plots in Fig. 3.1. The numerical results indicates that the maximum number of photon counts making position measurements occur when $r_2 = 0.577$, and the total number of photon counts does not appear to depend on the modulation amplitude parameter, $\beta$, for a device of constant refractive index and light wavelength. For a spiral phase plate etalon input parameters of $n = 1.556$, $\Delta h = 1.321\mu m$, $h_0 = 0.6cm$, and $\lambda = 632.991$nm, the value obtained for reflectivity is $r_2 = \frac{n-1}{n+1} = 0.217$, which results in an etalon finesse of $F = \frac{\pi r_2}{1-r_2^2} = 0.72$ indicating an ultra-low finesse device. The angular pattern modulation frequency of the transmission function is $\beta = 2n\frac{\Delta h}{\lambda} = 6.498$, giving rise to a minimum position resolution of $\delta R_{min} = 1.07\times10^{-4}$ rad as calculated

from Eq. 3.1. The position sensitivity of the etalon as a function of reflectivity is shown in Fig. 3.2(c). A factor to convert the position uncertainty to a frequency uncertainty is now calculated.

As the laser beam makes multiple reflections with the azimuthally varying surface of the spiral phase plate etalon fabricated with uniform refractive index, the phase that it acquires is $\varphi_h = \frac{\beta(\phi+\phi_0)}{2} = 2nk\left(h_0 + \Delta h\frac{\phi}{2\pi}\right)$. A change in laser frequency $\delta\nu$ with respect to the center laser frequency $\nu$ is equivalent to a small change in transmission function phase, $\delta\varphi_h$, with respect to the total phase acquired by the beam, $\varphi_h$,

$$\frac{\delta\nu_{Laser}}{\nu_{Laser}} = \frac{\delta\varphi_h}{\varphi_h}. \tag{3.5}$$

The base height, $h_0$ is engineered such that it is much larger than the azimuthal step height, $h_0 >> \Delta h$, and mathematically the base height does not change with azimuthal angle, $\delta h_0 = 0$, so the fractional change in frequency becomes

$$\frac{\delta\nu_{Laser}}{\nu_{Laser}} = \frac{\Delta h}{h_0}\frac{\delta\phi}{2\pi} \tag{3.6}$$

Hence the interference pattern will rotate by an angle, $\delta\phi$, as a function of a change in laser frequency $\delta\nu_{Laser}$:

$$\delta\phi = 2\pi\frac{h_0}{\Delta h}\frac{\delta\nu_{Laser}}{\nu_{Laser}}. \tag{3.7}$$

The angular position, $\delta R_{min}$, is converted to a frequency in units of Hertz using

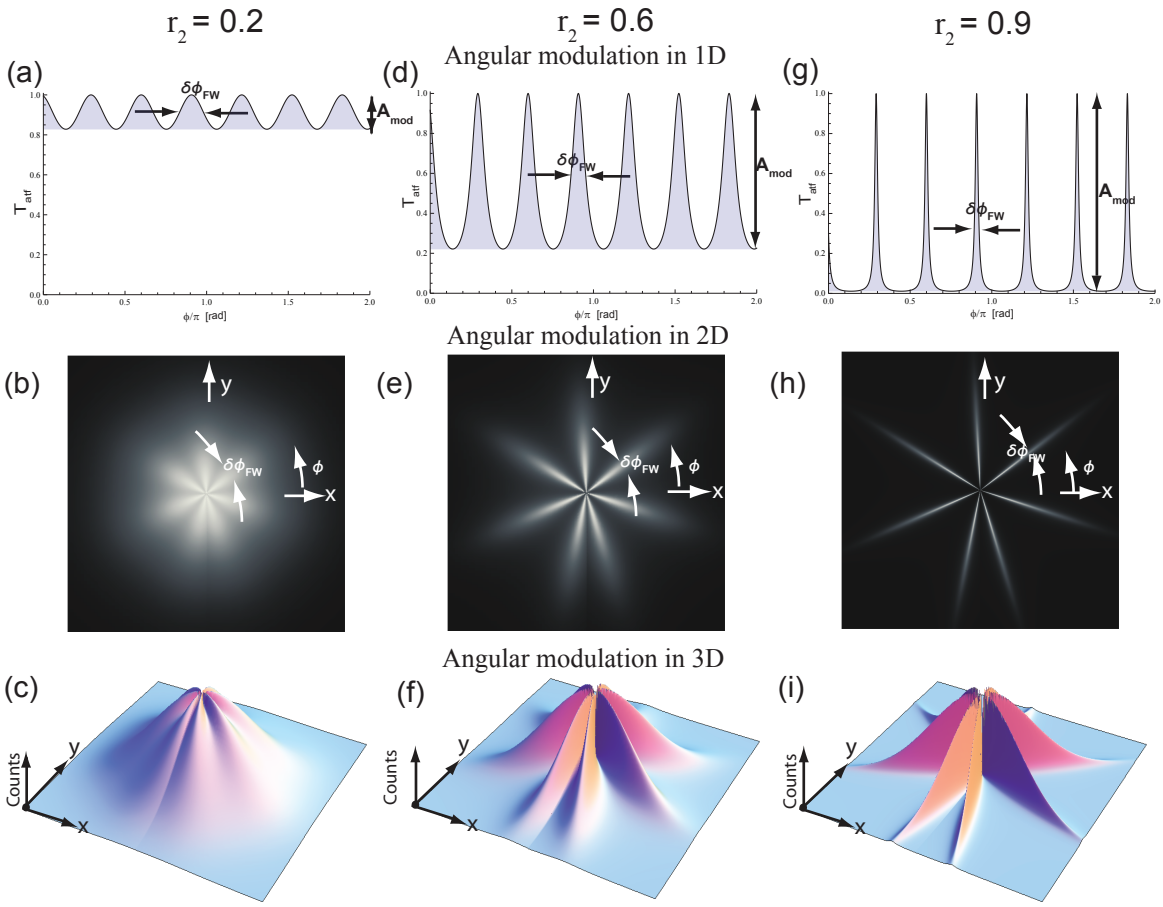


Figure 3.1: 1D, 2D, and 3D plots of theoretically calculated transmission through spiral phase plate in the thin plate approximation for reflectivity, $r_2 = 0.2$ (a)-(c), $r_2 = 0.6$ (d)-(f), and $r_2 = 0.9$ (g)-(i), respectively. The shaded region in the 1D plots show the region of the transmission function making position measurements on the CCD detector. The peak intensity used to generate 2D and 3D theoretical profiles is $I_0 = 5 \times 10^4$ counts with a $\frac{1}{e^2}$ beam waist of 1.9mm. The value of the modulation frequency is $\beta = 2n\frac{\Delta h}{\lambda} = 6.498$. The 2D plots is a view of the intensity profile in which all the azimuthal fringes can be seen unambiguously at the same time, and in real time and space on the CCD screen. Fig. 3.2 shows a plot of the transmission fringe width as a function of reflectivity as well as the number of photon counts making position measurements on the CCD detector as a function of reflectivity, which is used to determine a numeric value of the etalon sensitivity.

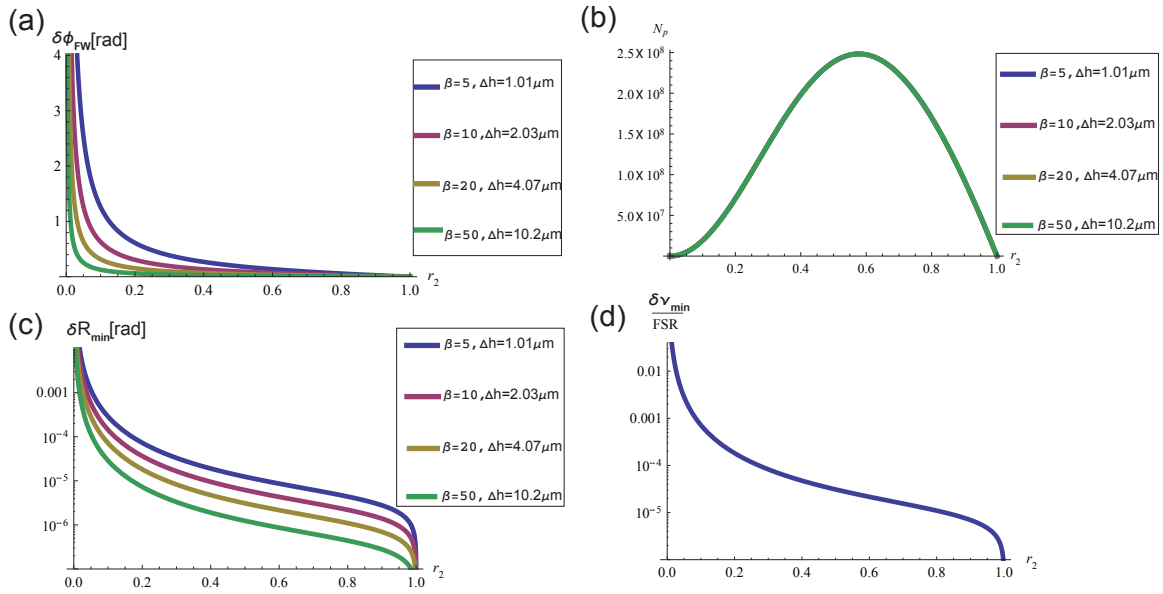


Figure 3.2: (a) Fringe width of transmission function as a function of reflectivity for different step heights which corresponds to different values of modulation frequency, $\beta$ of the angular interference pattern. (b) Number of photon counts making position measurements on the CCD detector as a function of reflectivity with a maximum at $r_2 = 0.577$. (c) The minimum sensitivity of the etalon in units of radians for different phase plate etalon step heights, $\Delta h$, as calculated in Eq. 3.1. (d) Minimum frequency sensitivity of the etalon normalized with the free spectral range of the etalon as calculated in Eq. 3.8. The frequency sensitivity does not appear to explicitly depend on $\beta$ as seen in Eq. 3.8(d). It appears to have a stronger dependence on reflectivity. These calculations are in the thin plate approximation, and as shown in section 2.3.1 of chapter II, the thin plate approximation starts to breakdown at around a reflectivity of $r_2 = 0.7$.

Eq. 3.7 to obtain a theoretically calculated frequency sensitivity of the etalon,

$$\delta\nu_{min} = \frac{\delta\phi}{2\pi}\frac{\Delta h}{h_0}\nu \tag{3.8a}$$

$$= \frac{\delta R_{min}}{2\pi}\frac{\Delta h}{h_0}\nu \tag{3.8b}$$

$$= \frac{1}{\sqrt{N_p}}\frac{1-r_2^2}{\pi r_2}\frac{2\pi}{\beta}\frac{\Delta h}{h_0}\nu \tag{3.8c}$$

$$= \frac{1}{\sqrt{N_p}}\frac{c}{2nh_0}\frac{1-r_2^2}{\pi r_2}. \tag{3.8d}$$

The free spectral range of the etalon is $FSR = \frac{c}{2nh_0}$. A plot of the frequency sensitivity in Eq. 3.8(d) normalized with the free spectral range (FSR) of the etalon is in Fig. 3.2(d). For the phase plate input parameters of $\Delta h = 1.321\mu m$, $h_0 = 0.6cm$, $\lambda = 632.991$nm, and $\beta = 6.498$ and $r_2 = 0.217$, the numeric value of the theoretically calculated frequency sensitivity of the etalon is 2.47MHz. The frequency sensitivity can also be related to the average lifetime of photon counts in the etalon derived in section 2.2.2 of chapter II,

$$\delta\nu_{min} = \frac{1}{\sqrt{N_p}}\frac{c}{2nh_0}\frac{1-r_2^2}{\pi r_2} \tag{3.9a}$$

$$= \frac{1}{\sqrt{N_p}}\frac{1}{2n}\frac{1}{\tau_{thin}}\left(\frac{1+r_2^4}{1-r_2^4}\right)\frac{1-r_2^2}{\pi r_2} \tag{3.9b}$$

$$= \frac{1}{\sqrt{N_p}}\frac{1}{\tau_{thin}}\left(\frac{1+r_2^4}{1+r_2^2}\right)\frac{1}{\pi 2nr_2}. \tag{3.9c}$$

As seen in Eq. 3.1, Eq. 3.8, Eq. 3.9, Fig. 3.1, and Fig. 3.2, the number of photon counts within the modulation amplitude of the angular interference pattern as well as the width of the etalon transmission fringes will play a role in determining the sensitivity of the etalon to rotation of the optical angular interference pattern. It also gives insight into the optimal phase plate parameters to improve the sensitivity of the pattern to rotation. Even though the maximum number of photon counts making

position (or frequency) measurements is at $r_2 = 0.577$ as seen in Fig. 3.2(b), it appears that this value does not necessarily correspond to the optimal sensitivity of the etalon. The optimal value is determined by the lifetime of the photon counts in the etalon as well as the number of photon counts making position (or frequency) measurements on the CCD detector. These numbers can be improved by either going to a longer etalon or increasing the reflectivity at the surfaces of the etalon. That is, with longer "photon" lifetime in the etalon, the azimuthally varying fringes are narrower and this enables the CCD detector to spatially distinguish a small rotation of the angular interference pattern [See Fig. 3.1 for 1D, 2D and 3D intensity profile]. As a result, the best values of sensitivity are obtained for large values of $r_2$ and $h_0$, as well as a very small free spectral range of the etalon. It has been assumed that the transmission function is in the thin plate approximation, and this approximation throughout this chapter. As shown in section 2.3.1 of chapter II, this approximation is valid up on to a reflectivity of $r_2 = 0.7$, after which there are noticeable deviations in the angular interference pattern described by the thick plate approximation. Hence, calculations in the thin plate approximation may not describe the phase plate accurately beyond a reflectivity of about $r_2 = 0.7$ (see fig. 2.7 in section 2.3.1 of chapter II). It must be noted that this applies to a fixed set of parameters, and it may be possible to still obtain better sensitivity to rotation of the optical angular interference pattern by going to higher reflectivity, but the device may not be described appropriately by the thin plate approximation. For the remainder of this dissertation, the spiral phase plate etalon is discussed in the context of an ultra-low finesse device in which the calculations in the thin plate approximations appear to be valid as shown in section 2.3.1 of chapter II.

## 3.3 Computer generated optical intensity

The optical intensity profile is simulated based on shot-noise limited assumptions in a Mathematica program, i.e. a computer generated optical intensity profile is produced based on shot-noise limited assumptions and analyzed. It is assumed that there is no fluctuation in photon counts due to the field's intensity and phase. Only the unavoidable noise from a distribution of photon counts as a result of the statistical nature of the quantum-mechanical detection mechanism is considered. This assumption is valid if each pixel of the CCD detector is integrated for a time that is long compared to the characteristic time scale of the fluctuation in intensity and phase such that the field's noise is averaged out (70; 71; 72). Shot noise is generally improved by using large number of photon counts on the CCD detector.

The optical vortex beam counts on the CCD are defined by the transmission function of the spiral phase plate etalon in the thin plate approximation and the spread in photon counts arriving at a single pixel is described by a Poisson distribution,

$$P\left(\mu, n_c\right) = \frac{\mu^{n_c}}{n_c!} e^{-\mu}. \tag{3.10}$$

This is the probability of detecting $n_c$ photon counts with mean photon counts, $\mu = T_{\text{atf}} I_0 e^{\frac{-2r^2}{\omega_0^2}}$, where $T_{\text{atf}}$ is the etalon transmission function [See Eq. 3.2], $I_0$ is the peak intensity, and $\omega_0$ is the $\frac{1}{e^2}$ beam waist. A built-in random integer generator in a Mathematica program is used to create the counts in each pixel. Similarly, the Gaussian laser beam counts has a intensity distribution, $I_0 e^{\frac{-2r^2}{w_0^2}}$, with a spread in photon count fluctuation also described by a Poisson distribution.

Four sets of images are generated: Gaussian beam on top of background counts, background counts alone, optical vortex beam on top of a background counts, and a second background counts alone [See fig. 3.3]. The fluctuation in background counts is described by Poisson statistics as well. The reason for generating background counts

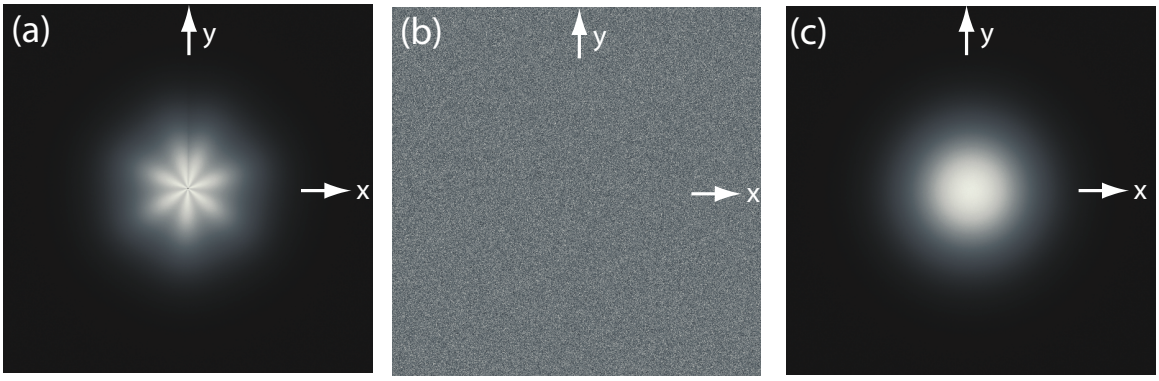


Figure 3.3: Computer generated data based upon shot noise limited assumptions. (a) Optical vortex counts for $\beta = 6.498$ on top of uniform background counts. (b) Uniform background counts. For actual analysis two sets of background counts are generated, one for the optical vortex laser beam and the other for the Gaussian laser beam. (c) Gaussian laser beam counts on top of uniform background counts.

is because the CCD used in the experiment have a constant off-set in background counts which needs to be subtracted out when analyzing the data. The 2D Gaussian laser beam center $(x_0, y_0)$ and $\frac{1}{e^2}$ beam waist, $\omega_0$, is found by integrating the row of x pixels and fitting it to a Gaussian function Bkg+$e^{\frac{-2(y+y_0)^2}{w_{0_y}^2}}$ to find $y_0$ and $w_{0_y}$. Bkg is the offset in background counts. Similarly, $x_0$ and $w_{0_x}$ is found by integrating the column of y pixels and fitting to a Gaussian function, Bkg+$e^{\frac{-2(x+x_0)^2}{w_{0_x}^2}}$. For a well characterized Gaussian laser beam, $w_{0_x} = w_{0_y}$.

As will be seen later, a pixel by pixel normalization is performed to the data, were all the vortex beam pixels is normalized with the corresponding Gaussian beam pixels. In order to do this effectively, vortex beam will have to be spatially overlapped properly with the Gaussian beam. A quantitative way of doing this is to ensure that the value of $x_0$ ($y_0$) of the Gaussian beam is the same as the value of $x_0$ ($y_0$) of the vortex beam. Different $x_0$ or $y_0$ will lead to an asymmetry in the peak of the modulation amplitude and modulation frequency of the angular interference pattern. For the purpose of verifying that the analysis program is working well, the hand

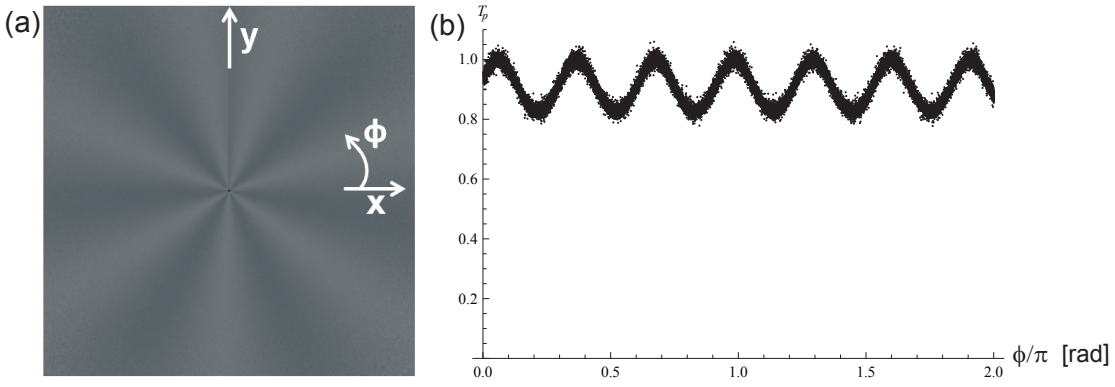


Figure 3.4: (a) 2D pixel by pixel normalization of transmission function described in Eq. 3.11. (b) Counts as a function of azimuthal angle. The transmission function, $T_p$, has a modulation frequency of $\beta = 6.498$ which corresponds to the number of azimuthally varying peaks.

selected $x_0$, $y_0$, $w_{0_x}$ and $w_{0_y}$ parameters to generate the data is used in the optical beam analysis program of this chapter.

In order to remove experimental artifacts or distortions in the input laser beam going through the phase plate during the experiment, a pixel by pixel normalization of the optical vortex laser beam with the Gaussian laser beam [See fig. 3.4 and fig. 3.5, Bottom] is performed,

$$T_p = \frac{N_V - N_{BV}}{N_G - N_{BG}}. \tag{3.11}$$

$N_V$, $N_G$, $N_{BV}$ and $N_{BG}$ are the counts in one pixel for the vortex beam, Gaussian beam, vortex background and Gaussian background, respectively. In addition, the optical angular modulation is generally clearly visible after performing the normalization. An angle $\phi$ is assigned to each value of the transmittance, $T_p$, in Eq. 3.11 on the CCD detector, and plotted as seen fig. 3.4(b).

For each beam, the transmission function in Eq. 3.11 is plotted as a function of angle, $\phi$. Caution is taken while assigning $\phi$ values to pixels close to the center of the optical beam as there will be one undefined $\phi$ point at the center and the neighboring pixels will have a large spread in angles for a few discrete $\phi$ values which

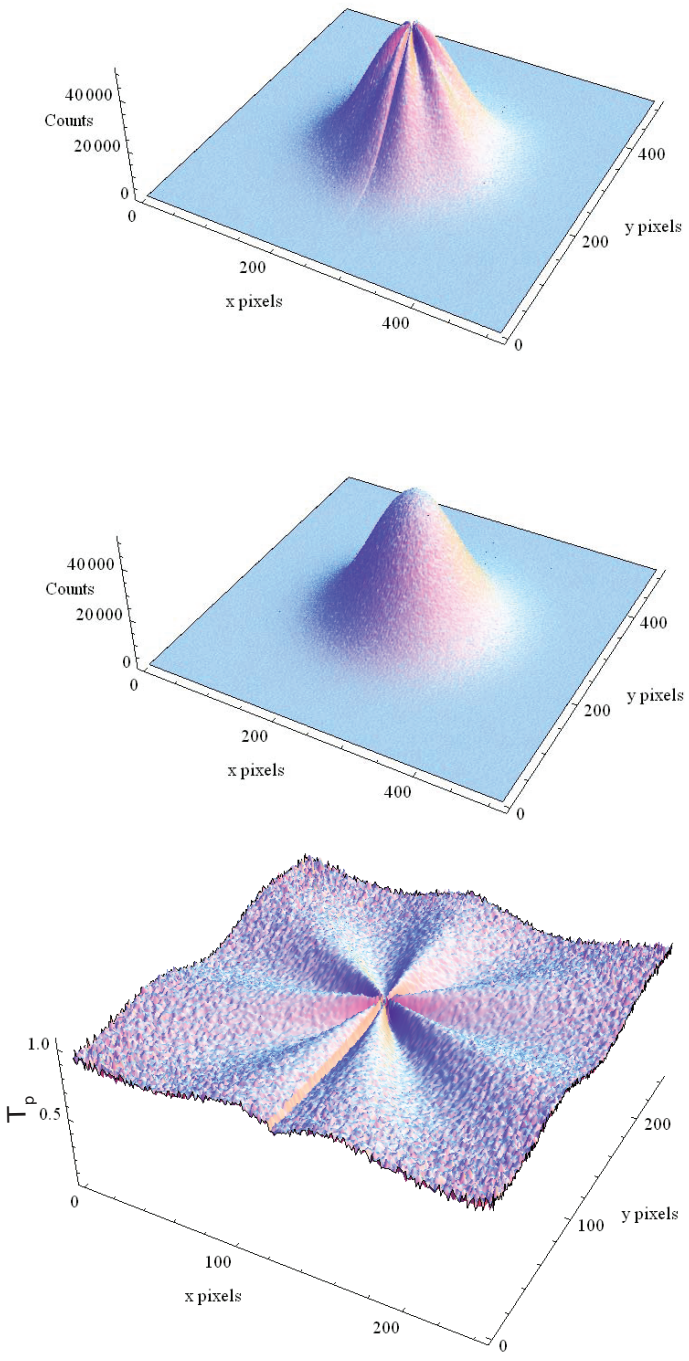


Figure 3.5: Computer generated data based upon shot noise limited assumptions. Top: 3D Optical vortex counts for $\beta = 6.498$ on top of uniform background counts. Contrast in angular fringes are sharper within the $\frac{1}{e^2}$ beam waist. Middle: 3D Gaussian laser beam counts on top of uniform background counts. Bottom: 3D pixel by pixel normalization of transmission function described by Eq. 3.11, which is integrated out to the the $1/e^2$ beam radius. The sharp contrast fringes can be seen clearly

may introduce systematic errors. Even though 99% of the intensity lie whithin $1.5w_0$, the data is integrated out to $1\omega_0$ which contain 86% of the beam intensity. This is because the interference fringes generally have sharper contrast within the $\frac{1}{e^2}$ beam waist(See fig. 3.5). The following section (Section 3.4) describes a method for putting error bars on each data point.

For the analysis in this chapter, the computer generated data has a $\frac{1}{e^2}$ Gaussian beam waist of approximately 1.9mm, and peak photon counts of approximately $5\times10^4$ on top of an average uniform background counts of $1.18\times10^3$. The integrated counts for the Gaussian beam is $\sum N_G = 1.12\times10^9$, Gaussian background is $\sum N_{BG} = 6.99\times10^7$, optical vortex counts is $\sum N_V = 1.03\times10^9$ and optical vortex background is $\sum N_{BV} = 6.99\times10^7$. A parameter to quantify the ratio of counts making position measurements to the total counts in the Gaussian laser beam is:

$$R_{VG} = \frac{(\sum N_G - \sum N_{BG}) - (\sum N_V - \sum N_{BV})}{\sum N_G - \sum N_{BG}} \tag{3.12}$$

The modulation amplitude of the optical vortex interference pattern is $A_{mod} = \frac{4r_2^2}{\left(1+r_2^2\right)^2} = 0.1718$ for a spiral phase plate etalon with uniform refractive index and a reflectivity of $r_2 = 0.217$. Since approximately $\frac{1}{2}A_{mod} = 0.0864$ is reflected back into the incoming Gaussian laser beam, and $\frac{1}{2}A_{mod} = 0.08649$ is transmitted into the optical vortex beam, the ratio in Eq. 3.12 is expected to be $R_{VG} = \frac{1}{2}\times0.1718 = 0.08649$. For this set of computer generated data, the ratio is calculated to be $R_{VG} = 0.08713$. Deviation of $R_{VG} = 0.08649$ from $A_{mod}$ in this set of computer generated data is expected to be from shot noise. This implies that if hundreds of images are generated, the average $R_{VG}$ extracted from the optical angular interference pattern would agree with $A_{mod}$ with a shot to shot fluctuation about the average $R_{VG}$. The relationship between $A_{mod}$ and $R_{VG}$ is used to determine the number of photon counts in the etalon since the experiment generally measures $A_{mod} = \frac{4r_2^2}{\left(1+r_2^2\right)^2}$ from the depth of the

optical angular interference pattern modulation.

To ensure that the program is working properly, analysis is performed on a non-integer vortex, $\beta = 6.498$, (See Fig. 3.4) as opposed to an integer $\beta$ vortex since a non-integer vortex incorporates many of the interesting features of integer vortices. In addition a spiral phase plate etalon with a non-integer $\beta$ is most likely to be used in the actual experiment.

## 3.4 Uncertainty in photon counts due to shot noise from each pixel on CCD screen

In this section, the uncertainty (error bar) is calculated from the transmittance of the spiral phase plate etalon. The counts in each pixel of the CCD camera for the vortex laser beam is $N_V$, Gaussian laser beam is $N_G$, optical vortex laser beam background is $N_{BV}$ and Gaussian laser beam background is $N_{BG}$. The transmission function for each pixel is computed as

$$T_p(N_V, N_{BV}, N_G, N_{BG}) = \frac{N_V - N_{BV}}{N_G - N_{BG}} \tag{3.13}$$

If $N_{Vbest}$, $N_{BVbest}$, $N_{Gbest}$, and $N_{BGbest}$, are the best estimates for $N_V$, $N_{BV}$, $N_G$, and $N_{BG}$, then the best estimate for the transmission function is expected to be $T_{pbest}(N_{Vbest}, N_{BVbest}, N_{Gbest}, N_{BGbest})$. An estimate of the uncertainty is obtained by expanding $T_p$ about the point $(N_V, N_{BV}, N_G, N_{BG})$ in a Taylor series. The first term in the Taylor expansion gives

$$T_p(N_V + \delta N_V, N_{BV} + \delta N_{BV}, N_G + \delta N_G, N_{BG} + \delta N_{BG}) \approx T_p(N_V, N_{BV}, N_G, N_{BG}) + \frac{\partial T_p}{\partial N_V}\delta N_V + \frac{\partial T_p}{\partial N_{BV}}\delta N_{BV} + \frac{\partial T_p}{\partial N_G}\delta N_G + \frac{\partial T_p}{\partial N_{BG}}\delta N_{BG} \tag{3.14}$$

Where $\delta N_V$, $\delta N_{BV}$, $\delta N_G$, $\delta N_{BG}$ are small increments in $N_V$, $N_{BV}$, $N_G$ and $N_{BG}$. The extreme probable values of $N_V$, $N_{BV}$, $N_G$, and $N_{BG}$ are $N_{Vbest} \pm \delta N_V$, $N_{BVbest} \pm \delta N_{BV}$, $N_{Gbest} \pm \delta N_G$, and $N_{BGbest} \pm \delta N_{BG}$, respectively. Substituting into Eq. 3.14, and taking the absolute values of the partial derivatives, the extreme values of $T_p$ is

$$T_p(N_{Vbest}, N_{BVbest}, N_{Gbest}, N_{BGbest}) \pm \left( \left| \frac{\partial T_p}{\partial N_V} \right| \delta N_V + \left| \frac{\partial T_p}{\partial N_{BV}} \right| \delta N_{BV} + \left| \frac{\partial T_p}{\partial N_G} \right| \delta N_G + \left| \frac{\partial T_p}{\partial N_{BG}} \right| \delta N_{BG} \right) \tag{3.15}$$

This means that the uncertainty of $T_p(N_V, N_{BV}, N_G, N_{BG})$ is

$$\delta T_p \approx \left| \frac{\partial T_p}{\partial N_V} \right| \delta N_V + \left| \frac{\partial T_p}{\partial N_{BV}} \right| \delta N_{BV} + \left| \frac{\partial T_p}{\partial N_G} \right| \delta N_G + \left| \frac{\partial T_p}{\partial N_{BG}} \right| \delta N_{BG} \tag{3.16}$$

If the uncertainties are random and independent, Eq. 3.16 is combined in quadrature (73; 74), and the following is obtained

$$\delta T_p = \sqrt{\left( \frac{\partial T_p}{\partial N_V} \delta N_V \right)^2 + \left( \frac{\partial T_p}{\partial N_{BV}} \delta N_{BV} \right)^2 + \left( \frac{\partial T_p}{\partial N_G} \delta N_G \right)^2 + \left( \frac{\partial T_p}{\partial N_{BG}} \delta N_{BG} \right)^2} \tag{3.17}$$

The equation describes the standard deviation of each pixel measuring the transmittance of the spiral phase plate etalon on the CCD screen. For counts in the optical intensity profile arriving at each pixel on the CCD screen and described by a Poisson distribution, the terms describing the uncertainty in Eq. 3.17 are $\delta N_V = \sqrt{N_V}$, $\delta N_{BV} = \sqrt{N_{BV}}$, $\delta N_G = \sqrt{N_G}$ and $\delta N_{BG} = \sqrt{N_{BG}}$. The analysis assumes that the standard deviation (uncertainty), $\delta T_p$ of each pixel (data point) is random with a 68% confidence level, i.e. $\delta T_p$ is to within 1 std. dev. of the "correct" value. The analysis has also assumed that systematic errors such as finding the center of the the optical vortex and gaussian laser beam is negligible compared to the random statistical errors discussed above. If the systematic errors $\delta T_{pSys}$ are comparable to random errors, then the standard deviation of each pixel will be $\sqrt{\delta T_p^2 + \delta T_{pSys}^2}$. The largest sources of systematic errors is expected to be from determining the center of

the optical beam profile to make plots of the transmittance as a function of angle, as well as from optical beam distortions.

## 3.5 Binning the raw data into angular wedges and estimating the uncertainty of each binned data point

The vortex optical intensity profile normalized with a Gaussian intensity profile shown in Fig. 3.4(b), is divided into angular wedges. The word "angular wedge" has a different meaning compared to chapter II. Previously, it meant a device with monotonically increasing thickness in a certain direction that has the shape of a triangle. In this chapter, it means partitioning the optical intensity profile of the beam as one would slice a round pizza into a series of triangular wedges. One slice of the pizza is one angular wedge, and it will be shown later in this section that the weighted sum of data points in an angular wedge represents one binned data point. When the optical intensity profile is plotted as a function of angle without dividing it into angular wedges, it is referred to as raw data. A plot of the binned data points is in Fig. 3.6(b), and a plot of the raw data points is in Fig. 3.4(b) and Fig. 3.6(a). The purpose of binning the raw data into angular wedges is to average out distortions in the optical angular interference pattern so that the data looks more presentable. This is especially advantageous when analyzing the experimental data as there are generally distortions in the optical intensity profile.

The weight given to each data point in the distribution for the raw data (unbinned data points) is $w_{T_{p_i}} = \frac{1}{\delta T_{p_i}^2}$, where $\delta T_{p_i}$ is given by Eq. 3.17. The index $i$ is used to denote the ith pixel on the CCD detector. The uncertainty in the transmittance through the spiral phase plate etalon containing $N_T$ total raw data points is

$$\delta T_T = \sqrt{\frac{1}{\sum_{i=1}^{N_T} w_{T_{p_i}}}} \tag{3.18}$$

The raw data points are partitioned into $x$ bins along the $\phi$ axis. If there are $k$ data points in an angular wedge, the new binned data point, $n_j$, is the weighted average of the k data points,

$$n_j = \frac{\sum_{i=1}^{k} T_{p_i} w_{T_{p_i}}}{\sum_{i=1}^{k} w_{T_{p_i}}}. \tag{3.19}$$

The index $j$ is to denote the $jth$ angular wedge (binned data point). The uncertainty of each binned data point (angular wedge) is

$$\sigma_{n_j} = \sqrt{\frac{1}{\sum_{i=1}^{k} w_{T_{p_i}}}} \tag{3.20}$$

The weight given to each binned data point (angular wedge) is $\frac{1}{\sigma_{n_j}^2}$, and will go into the fitting routine to better quantify the data. This is discussed in section 3.6 of this chapter. Since each binned data point (angular wedge) is a normal distribution [Fig. 3.6] of the unbinned data points within an angular wedge (one bin), the mean and standard error are reliable measures of random statistical uncertainties. If the individual bins are a normal distribution around the center but deviates at the edges, then analysis techniques such as the bootstrap method (75; 76; 77) is more reliable in quantifying the uncertainty. A recent example applying this type of analysis is in ref. (78) which reports on an improved measurement of the shape of an electron. The uncertainty for the binned data distribution is the weighted sum of all the uncertainties of the binned data points

$$\delta T_{n_T} = \sqrt{\frac{1}{\sum_{j=1}^{x} \frac{1}{\sigma_{n_j}^2}}} \tag{3.21}$$

Note that Eq. 3.18 and Eq. 3.21 should yield identical results if done appropriately. The numerical value obtained from Eq. 3.18 or Eq. 3.21 can serve as a measure of how close the experimental data is to its shot noise limited value by comparing the value obtained for the experimental data to the computer generated data. It appears

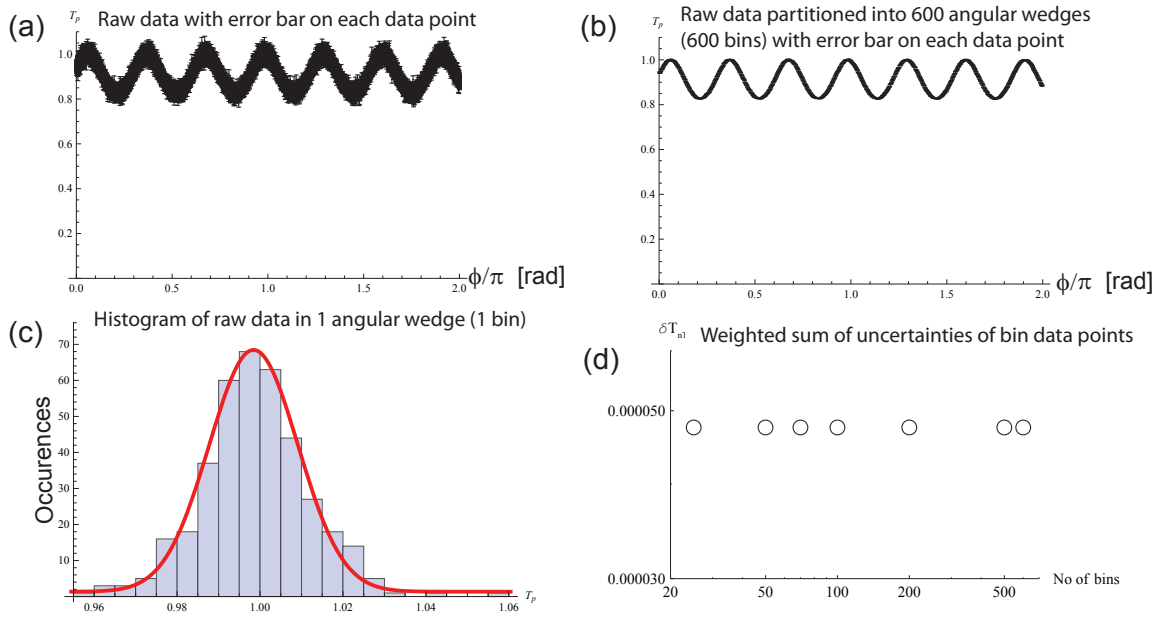


Figure 3.6: (a) Raw computer generated data from transmission function, $T_p$, with central values and error bars (uncertainty) defined by Eq. 3.13 and Eq. 3.17, respectively. (b) Raw data partitioned into 600 angular wedges (600 bins) with central value and error bar defined by Eq. 3.19 and Eq. 3.20, respectively. (c) Histogram of transmission function counts in one angular wedge of width $\Delta\phi = \frac{2\pi}{100}$ and red line is a Gaussian fit to the histogram with a 1 std. dev. width of 0.0107. (d) Square root of the weighted sum of error bars, $\delta T_{n_T}$, as derived in Eq. 3.21 vs number of bins (angular wedges).

to be a robust way of determining the shot noise limited value of the measurement.

An alternative method to determine the shot noise limit of the experimental measurements is to take a narrow angular slice of the transmitted counts through the spiral phase plate etalon over an angle, $\phi$, i.e. an angular wedge of the transmission function, make a histogram of the counts within the angular wedge, and fit it to a Gaussian function [See Fig. 3.6(c)]. The shot noise limit of the measurement can be obtained by comparing the 1 std. dev. Gaussian width for the computer generated data and experimental data. In this method, careful consideration must be taken in the choice of the angular slice as there may be other artifacts in the experimental data. In addition, the choice of bins used in constructing the histogram will affect its 1 std. dev. Gaussian width. In comparing the experimental and computer generated histogram, broadening in the experimental histogram width could be as a result of the detector not being shot noise limited or noise in the field's intensity and/or phase (See appendix C).

If the source of noise for photon counts in an angular wedge of the interference pattern is periodic or deviations from randomness, it could lead to significant deviations of the histogram of counts in an angular wedge resembling a normal distribution. This effect has been observed in the experimental data when using the Thorlabs CCD camera (DCU 200 series) (80) as a result of its digitization and read-out mechanism. Chapter IV discusses another way of quantifying the shot noise limit of the experiment through least square fitting of the computer generated data and comparing it to the experimental data. Least square fitting is discussed in section 3.6 of this chapter.

## 3.6 Spiral phase plate etalon sensitivity and parameters from least square fitting routine

The central values of the individual parameters ($r_2$, $A$, $\beta$, and $\phi_0$), and corresponding error bars are obtained from weighted fit of the computer generated data to the spiral phase plate etalon transmission function. The best fitting curve is determined by minimizing the weighted sum of the deviations from the fitting function through a Levenberg-Marquardt nonlinear least square minimization algorithm. A custom version of this algorithm in a mathematica program is used to perform the operation. The weights for each data point is determined from $w_{T_{p_i}} = \frac{1}{\delta T_{p_i}^2}$ or in the case of data points binned into angular wedges, the central value is given by Eq. 3.19 and weight is $w_{n_j} = \frac{1}{\sigma_{n_j}^2}$. As the bin size is changed, the individual fitting parameters and error bars should not depend on the bin size. This is because for fewer binned data points, the error bars will change by a similar factor. This serves as one of the cross-checks to ensure the proper functioning of the fitting routine. A second critical check is to ensure the reduced chi-square is $\chi_\nu^2 \approx 1$. A value of $\chi_\nu^2 >> 1$ may indicate poor measurements, incorrect assignment of uncertainty, or an incorrect choice of probability function. A $\chi_\nu^2 << 1$ may indicate an error in the assignment of weights to the data points or misunderstanding of the experiment (73).

The fitting function is

$$T(\phi) = \frac{A^{\text{CalcFit}}}{1 + \frac{4|r_2^{\text{CalcFit}}|^2}{(1-|r_2^{\text{CalcFit}}|^2)^2} \sin^2\left(\frac{\beta^{\text{CalcFit}}(\phi+\phi_0^{\text{CalcFit}})}{2}\right)}. \tag{3.22}$$

The standard error on the raw data and the binned data is expected to be within 1 std. dev. of each other for an appropriately selected bin number. 600 bins is selected in Fig. 3.7(b), for which the value is well within the 1 std. dev. level. The reduced chi-squared is $\chi_\nu^2 = 1.028$, and it is a value close to 1 for all the reported

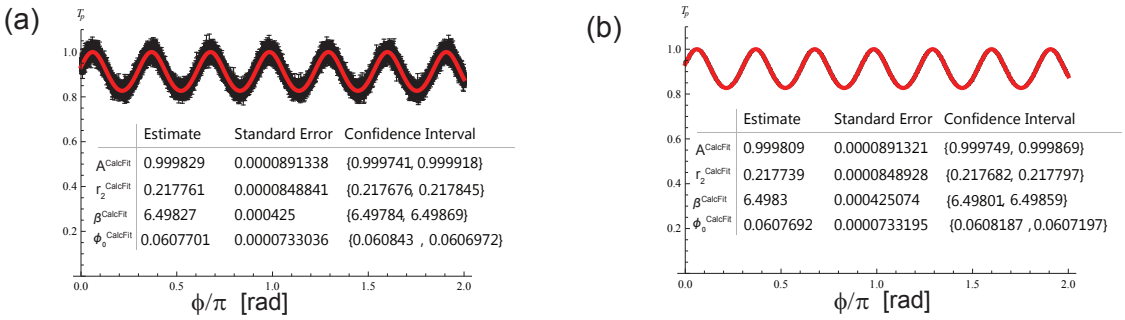


Figure 3.7: Calculated transmittance as a function of angle for raw computer generated data, i.e. unbinned computer generated data (a) and computer generated data which is binned into angular wedges(b). The error bars is due to the presence of shot noise in the data. The fit is performed in (a) to the raw computer generated data with fit parameters in the inset. In (b), the raw data is binned into 600 angular wedges (600 bins) with fit parameters in the inset. The red curve is a fit to the data. In the case of the binned data, the fit curve covers the data points. Fit parameters are in the 68% confidence interval. The fit parameters in both cases yield consistent results indicating proper functioning of the fit routine.

values of the fitting routine in this chapter. The $A^{\mathrm{CalcFit}}$ parameter can be normalized to 1 without loss of generality. The fit parameters $r_2^{\mathrm{CalcFit}} = 0.2177$ (1.1 std. dev.) and $\beta^{\mathrm{CalcFit}} = 6.4983$ (0.85 std. dev.) are relevant in determining properties of the spiral phase plate etalon. The quantity in parenthesis is the number of standard deviations (std. dev.) of the output fit parameters from the input parameters used to generate the shot-noise limited angular interference pattern. The position of the azimuthally varying fringe is determined from $\phi_0^{\mathrm{CalcFit}}$ with a position sensitivity at the $7.3 \times 10^{-5}\pi$rad level or converted to a frequency sensitivity of 3.98MHz using Eq. 3.8. $\phi_0^{\mathrm{CalcFit}} = (-0.0607 + 0.0766)\pi$ is one of the minimums of the fitted transmission function close to zero. More analysis of this fitted parameter is in the next subsection 3.6.1.

The sensitivity of the etalon is the error bar on the fitted parameter, $\phi_0$. As the transmission function is periodic in angle, there are multiple minimization values reported by the Levenberg-Marquardt algorithm which depends on the initial

search parameters. For example, a $\beta^{\text{CalcFit}} = 6.5$ will have 6 or 7 maximums in the transmission function amplitude.

As the computer generated data is free from instrumental artifacts, the fit to the transmission function of the shot to shot image is not expected to change by more than 3 std. dev. about the input central value. Furthermore, systematic errors resulting from finding the $x_0$ and $y_0$ center position of the optical beam is not included in the calculation of this chapter since the center position is known to a very high level of precision (i.e. the center position is hand selected). However, in analyzing the actual experimental data, such systematic errors will have to be considered in the error bar estimation. This will be seen in the analysis of the measured optical intensity profile of chapter IV.

### 3.6.1 Changing $\phi_0$

As $\phi_0$ is the parameter that is constantly being monitored in the experiment, special attention is given to this parameter in this section. In the experiment, $\phi_0$ is varied by changing the laser frequency which causes the interference pattern to rotate. It is important for $\phi_0$ to be reported within the predicted uncertainty as the angular position changes. In order to verify this, the position $\phi_0$ reported by the fit program is recorded as the hand selected input parameters is increased in steps of 0.1 rad from 0 rad to 2 rad for integer and non-integer values of $\beta$ (see Fig. 3.8). Fig. 3.9 and Fig. 3.10 contains a few images of the 2D intensity profile showing the rotation of the angular interference pattern. For integer values of $\beta$, the fitting routine reports the hand selected input value to within the program's uncertainty. However, for non-integer $\beta$, the value of $\phi_0^{\text{CalcFit}}$ had to be shifted by approximately $\frac{1}{2}\frac{2\pi}{\beta}$ to accurately report its value within the program's uncertainty ( Fig. 3.8 Top and Middle).

The minimums of the fitted transmission function is determined at a point $\phi_0 =$ 0.1rad and subtracted from a point $\phi_0 =$ 0rad as in Fig. 3.8 (Bottom). Since uncer-

tainties add in quadrature, performing this operation effectively increases the error bar on $\Delta\phi_0^{\text{CalcFit}}$ by at least a factor of $\sqrt{2}$. The central values is expected to be within 1 to 3 std. dev. of the hand selected difference in input values of the computer generated data. In Fig. 3.8 (Bottom), six independent minimization values of $\phi_0$ corresponding to the different modulation peaks are determined, all of which are within 1 std. dev. of the uncertainty. In the actual experiment, multiple measures of the value of $\phi_0$ will be recorded to determine the central value and error bar. A random distribution about the central value is expected as will be seen in the measurements and analysis of chapter IV

The etalon transmission function with $n_r$ maximums in its modulation amplitude is:

$$T(\phi) = \frac{1}{1 + \frac{4|r_2|^2}{(1-|r_2|^2)^2}\sin^2\left(\frac{\beta(\phi+\phi_0)}{2} + n_r\pi\right)} \tag{3.23a}$$

$$= \frac{1}{1 + \frac{4|r_2|^2}{(1-|r_2|^2)^2}\sin^2\left(\frac{\beta(\phi+\phi_0+\frac{2n_r}{\beta})}{2}\right)} \tag{3.23b}$$

$$= \frac{1}{1 + \frac{4|r_2|^2}{(1-|r_2|^2)^2}\sin^2\left(\frac{\beta(\phi+\phi_{0_{n_r}})}{2}\right)}. \tag{3.23c}$$

If $\phi_0$ is the first maximum of the transmission function, the transmission peaks will repeat itself at $\phi_{0_{n_r}} = \phi_0 + \frac{2n_r\pi}{\beta}$, where $n_r$ is an integer. An etalon with integer $\beta$ will have $n_r = \beta$ maximums and $n_r = \beta$ minimums, while an etalon with non-integer $\beta$ will have $n_r = Ceiling[\beta]$ maximums and $n_r = Floor[\beta]$ minimums, or vice versa. For an appropriate shift in angular phase, $\phi_{0_{n_r}} = \phi_0 + \frac{2n_r\pi}{\beta}$, the interference pattern reproduces itself within a $2\pi$ radian angle. This is one of the unique geometric features of the spiral phase plate etalon that differs from the conventional Fabry-Perot etalon consisting of longitudinal modes. Typically, the interference pattern rotates through a $2\pi$ radian angle when the laser frequency is changed by approximately $\delta\nu \approx 100$GHz,

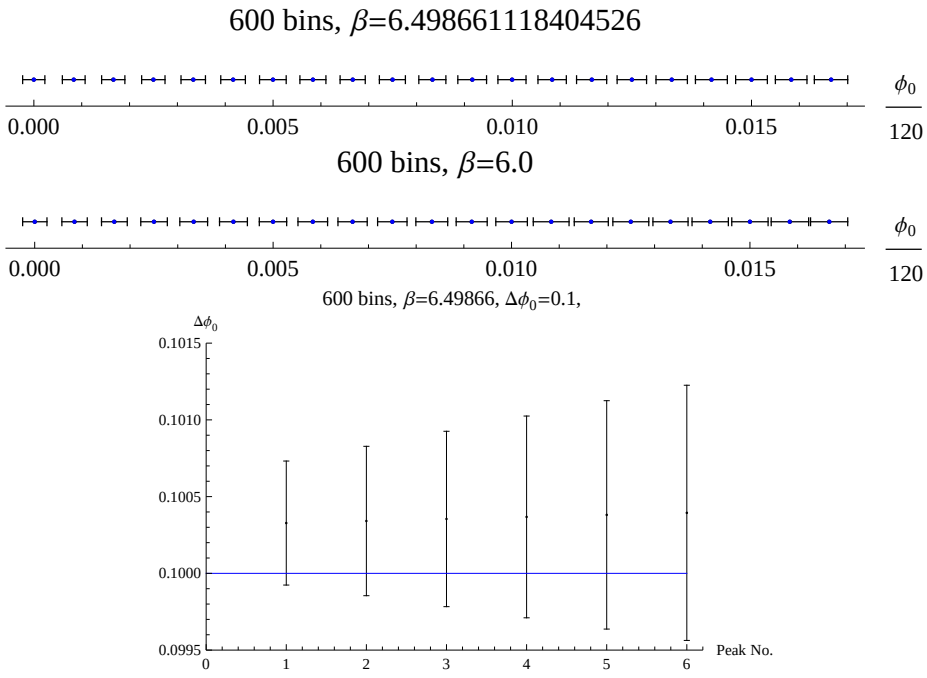


Figure 3.8: Top: Value of $\phi_0$ for $\beta = 6.49866$ varied from 0 rad to 2 rad in increments of 0.1rad. The values of $\phi_0$ is normalized by a factor of 120 to give a closer look at the error bars. Middle: Same as top but for $\beta = 6.0$. Blue dots are the hand selected input values and black is the output from the fitting routine. In both cases, blue dots overlap very well with black dots indicating very good agreement of fitting routine values and hand selected values. Bottom: Verifying that a change in angular position of $\Delta\phi_0 = 0.1$ radian in the computer generated data yields a similar change of $\Delta\phi_0^{\text{CalcFit}} = 0.1$ radian in the value reported by the fit program for 6 different minimization peaks in a single shot image. Blue line correspond to hand selected theoretical change in $\phi_0$

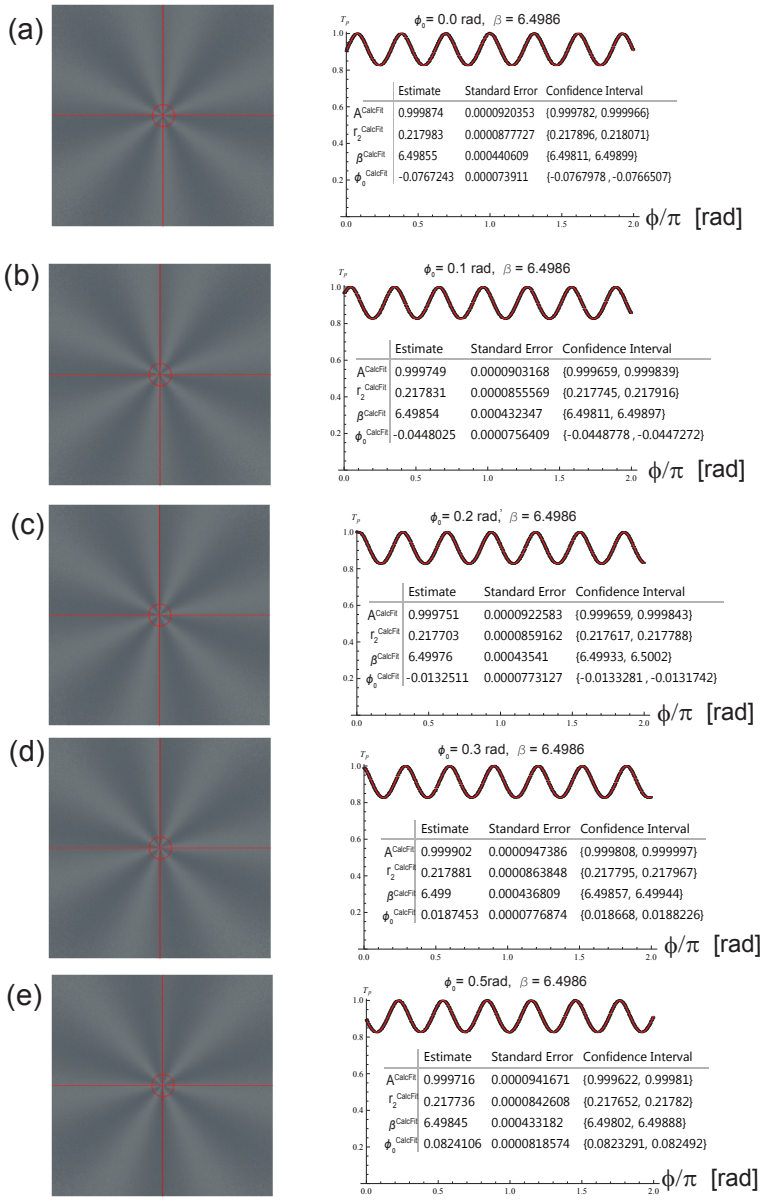


Figure 3.9: Pixel by pixel normalization of the optical vortex with Gaussian beam (described by Eq. 3.13) for a $\beta = 6.4986$ when the value of $\phi_0$ is changed from 0 rad to $0.5\pi$ radian. Beside each 2D image is data binned into 600 angular wedges and fit to Eq. 3.22, with the fit parameters in the inset. A full rotation of the interference pattern corresponds to a change of $\phi_0$ by $2\pi$ radian. The red cross bar is used to find the center of the 2D image to create the transmittance vs angle.

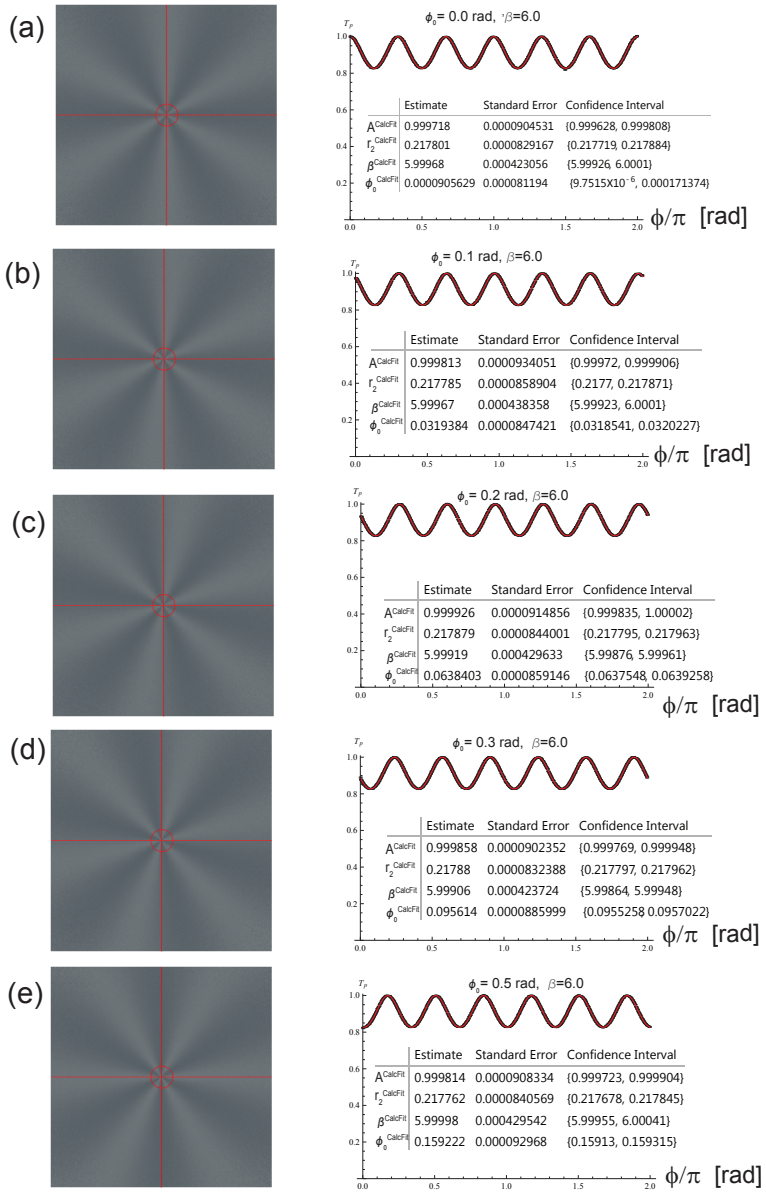


Figure 3.10: Pixel by pixel normalization of the optical vortex with Gaussian beam (described by Eq. 3.13) for a $\beta = 6.0$ when the value of $\phi_0$ is changed from 0 rad to $0.5\pi$ radian. Beside each 2D image is data binned into 600 angular wedges and fit to Eq. 3.22, with the fit parameters in the inset. A full rotation of the interference pattern corresponds to a change of $\phi_0$ by $2\pi$ radian. The red cross bar is used to find the center of the 2D image to create the transmittance vs angle.

with a free spectral range (i.e. frequency separation between two angular peaks) given by $\frac{\delta\nu}{\beta} = 16\text{GHz}$. For example, considering the parameters in this chapter to fabricate a $\beta = 6.4986$ spiral phase plate etalon, the laser frequency changes by $\delta\nu = 104\text{GHz}$ to rotate the interference pattern by a $2\pi$ radian angle. As such, the etalon can be tuned from a few MHz to 10's of GHz indicating a wide tunability in frequency.

### 3.6.2 Nonlinear least square fitting

In this section, the nonlinear fitting routine which performs a weighted fit to the optical angular interference pattern is described. The fitting routine calculates a value of $\chi^2$ that minimizes the sum of deviations of the data from the transmission function with respect to the parameters, $r_2$, $A$, $\beta$ and $\phi_0$,

$$\chi^2 = \sum w_i \left[T_i - T\left(\phi_i\right)\right]^2. \tag{3.24}$$

The weight of each data point is $w_i = \frac{1}{\sigma_i^2}$, and it has been derived in section 3.5. The derivatives to minimize $\chi^2$ are

$$\frac{\partial\chi^2}{\partial A} = 0, \quad \frac{\partial\chi^2}{\partial r_2} = 0, \quad \frac{\partial\chi^2}{\partial\beta} = 0, \quad \frac{\partial\chi^2}{\partial\phi_0} = 0. \tag{3.25}$$

A built in function in a Mathematica program is used to simultaneously solve Eq. 3.25. When analyzing the data, the values of $\chi^2$, the central values, and parameter error bars are obtained using two independent built-in functions in Mathematica: the *NonlinearModelFit* routine and *NMinimize* routine, in which the Levenberg-Marquardt algorithm and Differential Evolution method is used to find the fit parameters, respectively. These two fitting methods serve as independent cross-checks to show that the central values and error bars are consistent with the hand selected input computer generated values. However, for large number of data points (e.g. $10^5$ data points which is generally the case for the raw data), the *NonlinearModelFit* routine tends to

be computationally more time efficient. The central values and error bars reported by both fitting routines generally agree with each other to well within 1 std. dev.

The built-in *NonlinearModelFit* fitting routine in Mathematica is:

nlm =*NonlinearModelFit*[Data, $T(\phi, A^{\text{CalcFit}}, r_2^{\text{CalcFit}}, \beta^{\text{CalcFit}}, \phi_0^{\text{CalcFit}})$, $\{\{A^{\text{CalcFit}}, 1.0\}$, $\{r_2^{\text{CalcFit}}, r_2\}$, $\{\beta^{\text{CalcFit}}, \beta\}$, $\{\phi_0^{\text{CalcFit}}, \phi_0\}\}$, $\phi$, *ConfidenceLevel*$\rightarrow$ 0.68, *VarianceEstimatorFunction*$\rightarrow$ (1&), *Weights*$\rightarrow w_i$, *Method*$\rightarrow$ "LevenbergMarquardt"]

and the tabulated estimate of central values, standard errors and confidence intervals are obtained with the built-in function:

nlm["ParameterConfidenceIntervalTable"].

A few examples of sample output from the program is in Fig. 3.7, Fig. 3.9, Fig. 3.10 and Fig. 3.11(a). The command, "*VarianceEstimatorFunction*$\rightarrow$ (1&)", ensures that the fit program calculates the standard error of the fit parameters from the weights alone such that $\chi^2_\nu$ is normalized to 1. Similar fit parameters and standard errors are obtained without this setting for the computer generated data.

The built-in *NMinimize* fitting routine in Mathematica is:

*NMinimize*[ $\{\chi(, A^{\text{CalcFit}}, r_2^{\text{CalcFit}}, \beta^{\text{CalcFit}}, \phi_0^{\text{CalcFit}})^2,\ 1-\epsilon \leq A^{\text{CalcFit}} \leq 1+\epsilon,\ r_2 - \epsilon \leq r_2^{\text{CalcFit}} \leq r_2+\epsilon,\ \beta-\epsilon \leq \beta^{\text{CalcFit}} \leq \beta+\epsilon,\ \phi_0-\epsilon \leq \phi_0^{\text{CalcFit}} \leq \phi_0+\epsilon\ \}$, $\{A^{\text{CalcFit}}, r_2^{\text{CalcFit}}, \beta^{\text{CalcFit}}, \phi_0^{\text{CalcFit}}\}$, *Method*$\rightarrow$ "DifferentialEvolution"]

$\epsilon$ is a small deviation from the input computer generated parameters $r_2$, $\beta$ and $\phi_0$. The resulting fit parameters are $A^{\text{CalcFit}}$, $r_2^{\text{CalcFit}}$, $\beta^{\text{CalcFit}}$, and $\phi_0^{\text{CalcFit}}$. A sample output from the *NMinimize* routine is

{612.803, $\{A^{\text{CalcFit}}\rightarrow$ 0.999811, $r_2^{\text{CalcFit}}\rightarrow$0.217742, $\beta^{\text{CalcFit}}\rightarrow$ 6.49828, $\phi_0^{\text{CalcFit}}\rightarrow$-0.0607764}}

where $\chi^2 = 612.803$, and the reduced Chi-Squared is $\chi^2_\nu = 1.028$ for $\nu = 596$ degrees of freedom. It must be noted that in order to obtain the error bar from the *NMinimize* fit routine, a fit will have to be performed on several optical angular interference patterns and a histogram of the fit parameter distribution obtained. The 1 std. dev. width of

the histogram is the error bar. When this is done, these central value and error bar generally agree to well within the error bar generated by the *NonlinearModelFit* fit routine.

For shot-noise limited computer generated data with no artifacts in the optical intensity profile, it is not necessary to perform a weighted fit to the angular interference pattern in order to improve the error on the parameters reported by the fitting routine. This is because the angular interference pattern data points will have similar weights within $\frac{1}{e^2}$ beam waist of the vortex counts normalized with the Gaussian intensity profile discussed earlier in the chapter, especially when the peak intensity counts of the optical intensity beam profiles is as large as the ones reported in this chapter. However, in the case of the experimental data analysis, the precision to which the fit program reports the uncertainty of the fit parameters can be improved by performing a weighted fit to the experimental data. This is because there are generally artifacts in the measured optical intensity profile in which the weight on each data point can vary significantly. The purpose of performing the weighted fit is to ensure that the "good" data points have a higher weight than the "bad" data points. This is implemented when analyzing the experimental data in chapter IV.

### 3.6.3 Correlation in fit parameters

The different parameters reported by the fitting routine are correlated with each other. The correlation between the fit parameters is a measure of how much the minimization of one fit parameter is affected by another fit parameter while minimizing $\chi^2$ in the nonlinear fitting routine. A correlation of 1 indicates perfect correlation, while a correlation of 0 indicates no correlation. Typical central values, standard error, confidence interval and correlation matrix reported by the fitting routine is in Fig 3.11. There is a high degree of correlation between the amplitude parameters, $A^{\mathrm{CalcFit}}$ and $r_2^{\mathrm{CalcFit}}$ of 0.809. There is also a high degree of correlation between the phase param-

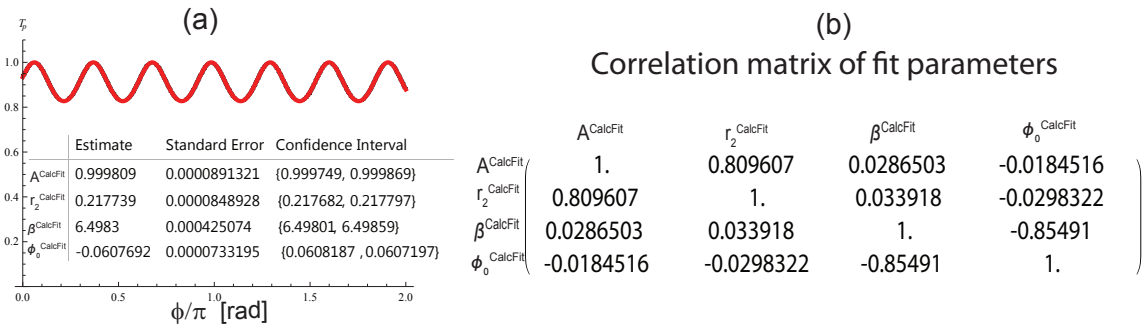


Figure 3.11: (a) Weighted fit to the binned computer generated data, with the fit parameters in the inset, and (b) correlation in the fit parameters. Correlation between $\beta^{\text{CalcFit}}$ and $\phi_0^{\text{CalcFit}}$ is 0.85, and correlation between $A^{\text{CalcFit}}$ and $r_2^{\text{CalcFit}}$ is 0.80. The other fit parameters are minimally correlated with each other.

eters $\beta^{\text{CalcFit}}$ and $\phi_0^{\text{CalcFit}}$ of 0.8542. The other parameters appear to be minimally correlated with respect to each other. Even though, $\beta^{\text{CalcFit}}$ and $\phi_0^{\text{CalcFit}}$ are highly correlated, it does not appear to affect the central values reported by the fitting routine to within its uncertainty (See fig. 3.8 Top and middle plots) as $\phi_0$ is varied. The fit parameters in the sub-section on "Changing $\phi_0$", assumes that $\phi_0$ is independent of $\beta$. In the experiment, varying $\phi_0$ by changing the laser frequency changes $\beta$ at the level of $\delta\beta = \beta\frac{\delta\nu}{\nu}$. Considering the parameters to fabricate a $\beta = 6.498$ phase plate, a change in laser frequency of $\delta\nu = 16$GHz about the central frequency $\nu = 473.9$THz, will result in $\delta\beta \approx \beta\frac{\delta\nu}{\nu} = 2.2 \times 10^{-4}$. The purpose of calculating the correlation in fit parameters is to ensure that the program does not introduce additional dependences of $\beta$ on $\phi_0$ or vice versa during the $\chi^2$ minimization process which would make data interpretation cumbersome.

While the correlation in the fit parameters merely contribute systematic errors for the parameters that are highly correlated, these systematic errors appear to be much smaller than errors due to shot noise, optical beam distortions, and finding the center of the optical beam. The major source of systematic errors are expected to be from finding the center of the beam to generate the azimuthally varying optical

intensity profile, and optical beam distortions. Such systematic errors are analyzed for computer generated data in section 4.2.6 of chapter IV.

## 3.7 Concluding remarks

In this chapter, a classical description of the minimum resolution to measure the rotation of an angular interference pattern in a spiral phase plate etalon has been discussed. In particular, the resolution of the angular pattern was estimated by:

1. Calculating the standard error of the number of photon counts making position measurements on the CCD, and

2. Through a weighted nonlinear least square fit of the computer generated data.

Fitting the data appears to be the most robust way of determining the spiral phase plate parameters and corresponding error bars, and it is used to estimate the experimental parameters and uncertainty in the proceeding chapters. A number of cross-checks were performed on the experimental data to ensure that the analysis programs are working properly. Two different custom algorithms (i.e. the Levenberg-Marquardt algorithm and difference evolution algorithm) was used to obtain the fit central values and error bars to ensure consistency of the values with hand selected input values to generate the data. In addition, the correlation between the different fit parameters was calculated to ensure that the fitting routine does not introduce additional dependences on the different fit parameters which would make data interpretation cumbersome. Systematic errors which the correlation in fit parameters may introduce are much smaller than other sources of errors in the experimental data, such as shot noise, etc.

Estimating the sensitivity of the device from a theoretically calculated standard error provides insight as to how the device sensitivity to rotation could be improved. In particular, the sensitivity of the angular interference pattern to rotation is expected